# Heliyon

CrossMark

# Effects of soil erosion and anoxic–euxinic ocean in the Permian–Triassic marine crisis

Kunio Kaiho [a,*], Ryosuke Saito [a], Kosuke Ito [a], Takashi Miyaji [a], Raman Biswas [a], Li Tian [b], Hiroyoshi Sano [c], Zhiqiang Shi [d], Satoshi Takahashi [a], Jinnan Tong [b], Lei Liang [b], Masahiro Oba [a], Fumiko W. Nara [e], Noriyoshi Tsuchiya [e], Zhong-Qiang Chen [b]

[a] *Department of Earth Science, Graduate School of Science, Tohoku University, Sendai, Japan*

[b] *State Key Laboratory of Biogeology and Environmental Geology, China University of Geosciences, Wuhan, China*

[c] *Department of Earth and Planetary Sciences, Kyushu University, Fukuoka, Japan*

[d] *Chengdu University of Technology, Chengdu, China*

[e] *Graduate School of Environmental Studies, Tohoku University, Sendai, Japan*

* Corresponding author.

E-mail address: kaiho@m.tohoku.ac.jp (K. Kaiho).

## Abstract

The largest mass extinction of biota in the Earth's history occurred during the Permian–Triassic transition and included two extinctions, one each at the latest Permian (first phase) and earliest Triassic (second phase). High seawater temperature in the surface water accompanied by euxinic deep-intermediate water, intrusion of the euxinic water to the surface water, a decrease in pH, and hypercapnia have been proposed as direct causes of the marine crisis. For the first-phase extinction, we here add a causal mechanism beginning from massive soil and rock erosion and leading to algal blooms, release of toxic components, asphyxiation, and oxygen-depleted nearshore bottom water that created environmental stress for nearshore marine animals. For the second-phase extinction, we show that a soil and rock erosion/algal bloom event did not occur, but culmination of anoxia–euxinia in intermediate waters did occur, spanning the second-phase extinction. We investigated sedimentary organic molecules, and the results indicated a peak of a massive soil erosion proxy followed by peaks of marine productivity proxy. Anoxic proxies of surface sediments and water occurred in the

shallow nearshore sea at the eastern and western margins of the Paleotethys at the first-phase extinction horizon, but not at the second-phase extinction horizon. Our reconstruction of ocean redox structure at low latitudes indicates that a gradual increase in temperature spanning the two extinctions could have induced a gradual change from a well-mixed oxic to a stratified euxinic ocean beginning immediately prior to the first-phase extinction, followed by culmination of anoxia in nearshore surface waters and of anoxia and euxinia in the shallow-intermediate waters at the second-phase extinction over a period of approximately one million years or more. Enhanced global warming, ocean acidification, and hypercapnia could have caused the second-phase extinction approximately 60 kyr after the first-phase extinction. The causes of the first-phase extinction were not only those environmental stresses but also environmental stresses caused by the soil and rock erosion/algal bloom event.

Keywords: Earth science, Environmental science, Geochemistry, Geology

## 1. Introduction

The largest mass extinction of eukaryotic biota in the Earth's history occurred at the Permian-Triassic (P/Tr) transition. It initiated the turnover of the biosphere from Paleozoic fauna to Modern fauna, including the dinosaurs, birds, and mammals. Two pulses of marine extinction took place in the latest Permian (first-phase extinction; Bed 25 of the Meishan section; 251.941 ± 0.037 Ma; Burgess et al., 2014) and earliest Triassic (second-phase extinction; Bed 28 of the Meishan section; 251.880 ± 0.031 Ma; Song et al., 2013; ages are revised after Burgess et al., 2014). A high-resolution study by Kaiho et al. (2006) showed that the latest Permian extinction occurred at 2 cm beneath the base of Bed 25 at Meishan. Siberian volcanism was the most likely cause; however, the direct causal mechanism for the biotic crisis has long been disputed. Direct causes that have been proposed include hypercapnia (physiological effects of elevated $P_{CO2}$; Knoll et al., 2007), the development of anoxic–suboxic or euxinic waters in the ocean including hydrogen sulfide ($H_2S$) release from the intermediate to surface water (Gorjan et al., 2007; Kaiho et al., 2012) and/or atmosphere (Kump et al., 2005; Kaiho et al., 2012; Kaiho and Koga, 2013), a decrease in atmospheric oxygen ($O_2$) (small contribution; Kaiho and Koga, 2013), an increase in temperature (Joachimski et al., 2012; Sun et al., 2012; Brand et al., 2012; Schobben et al., 2014), narrowing of the refuge zone by lethally hot surface water and euxinic deep-intermediate waters (Song et al., 2014), ocean acidification (Payne et al., 2010; Clapham and Payne, 2011; Payne and Clapham, 2012; Clarkson et al., 2015), terrestrial acidification (Sephton et al., 2015), and depletion of bioessential elements throughout the oceans (Takahashi et al., 2014).

A role of the development of anoxic-suboxic or euxinic (sulfide-bearing) deep and intermediate seawaters in the P/Tr mass extinction (Grice et al., 2005; Takahashi et al., 2014; Feng and Algeo, 2014) has been supported by the detection of small pyrite framboids and high concentrations of molybdenum (Mo), uranium (U), and vanadium (V) in deep-sea sedimentary rocks from that period in the central Panthalassic Ocean, indicating that the deep ocean was depleted of oxygen (Wignall et al., 2010; Algeo et al., 2010; Algeo et al., 2011; Takahashi et al., 2014). Algeo et al. (2010) estimated the redox conditions of deep water in the central Panthalassic Ocean during the latest Permian and earliest Triassic using the degree of pyritization (Raiswell et al., 1988), which indicated dysoxic conditions. Takahashi et al. (2014) provided evidence of euxinic conditions (accumulation of Mo, U, and V) in the deep waters of the central Panthalassic Ocean immediately before and during the latest Permian extinction. There is an abundance of data indicating oxic, dysoxic, and anoxic shallow waters during the latest Permian extinction in the Paleotethys (Cao et al., 2009; Kaiho et al., 2012; Brand et al., 2012). Most recently, Xiang et al. (2016) demonstrated oxic and Wang et al. (2016) reported dysoxic conditions in low-latitude shallow waters during the latest Permian extinction. However, the effects of the inflow of oxic material from land to sea and a lack of redox data on the surface waters of the Panthalassic Ocean have prevented reconstruction of the redox structure of the P/Tr ocean. Consequently, the ocean redox structure throughout the water column has yet to be determined.

Knoll et al. (2007) emphasized that $O_2$ deficiency in the ocean would not trigger such an extinction and would not likely lead to a widespread die-off. $O_2$ deficiency in shallow waters can also be ruled out as the primary kill mechanism given the high partial pressure of $O_2$ in the Phanerozoic atmosphere. Alternatively, euxinia of the marine photic zone developed in the surface ocean ($<24$ m) more often in the Phanerozoic than was previously thought (French et al., 2015).

In this study, we investigated soil and mud intrusion into the shelf and deep ocean, marine productivity in the shelf, and bioessential element levels spanning the two extinctions using sedimentary organic biomarker proxies at low latitudes. We also reconstructed the vertical redox structure using sedimentary organic biomarker proxies, redox-sensitive elements, and the morphology of pyrites at low latitudes. Our results indicate a massive soil and rock erosion event and marine productivity maxima accompanied by loss of bioessential elements in shallow waters and deficiencies of $O_2$ in surface sediment at the latest Permian extinction. The massive soil intrusion and algal blooms supported by huge nutrient inputs into the seas can explain the discrepancy between the $O_2$ deficiency in the surface sediment and the high partial pressure of $O_2$ in the Phanerozoic atmosphere because a massive accumulation of eroded sediments and dead algae would have caused $O_2$ deficiency in the surface sediments. These results should modify current views on the mechanism of the latest Permian extinction event to reflect a high flux of

soil and inorganic nutrients, leading to algal blooms and the depletion of bioessential elements in surface waters. The former process can in part be seen today, as algal blooms regularly lead to the release of toxic components, asphyxiation, intermittent deficiencies, and marine life mortality. The proposed events could have occurred globally owing to the devastation of land plants. Here, we add these events to the seawater temperature increase, pH decrease, hypercapnia, and expansion of euxinic–anoxic deep-intermediate waters as direct causes of the first-phase extinction. Our data show no soil and rock erosion/algal bloom event in the second-phase extinction, which indicates that such an event occurred only at the first-phase extinction. Our reconstruction of vertical ocean redox structure supports the idea of a narrowing of the refuge zone due to lethally hot surface water and euxinic deep-intermediate waters at the second-phase extinction as described by Song et al. (2014).

## 1.1. Geological setting

We investigated 11 sedimentary sections that contain the P/T interval, including: seamount carbonates in the central Panthalassic Ocean at Kamura, Japan; inner-shelf shallow-platform carbonate facies in the Palaeotethys Ocean at Bulla, Italy, and Dajiang, South China; middle-shelf carbonate facies with mudstone in the lower Griesbachian, below shallow platforms at Huangzhishan, Bianzhonglu, and Meishan, South China; outer-shelf mudstone facies at the Opal Creek section, western Canada (Schoepfer et al., 2013); upper-slope mudstone and carbonate facies at Shangsi, South China; and deep-sea chert-shale facies in Ubara, Akkamori, and Gujohachiman, Japan (Takahashi et al., 2009; Algeo et al., 2010; Kasuya et al., 2012). The studied sections were situated at low latitudes (Ziegler et al., 1998; Schoepfer et al., 2013; Takahashi et al., 2009; Algeo et al., 2010; Kasuya et al., 2012; Fig. 1).

To illustrate ocean redox structure in a figure, we set the approximate paleo-water depths of these sections as follows, based on fossils and lithology (Chen et al., 2010; Chen et al., 2011; Tian et al., 2014): ~10 m for Bulla, because of the presence of oolites and carbonate facies; ~30 m for Dajiang and Kamura, because of the presence of microbialite and carbonate facies; ~60 m for Huangzhishan, because of the dominance of carbonate and mudstone facies with brachiopods; and ~100 m for Bianzhonglu and Meishan, because of the carbonate and mudstone facies. The water depth for Shangsi was estimated to be 200–300 m based on its slump structure in the middle Griesbachian limestones and its dark cherty limestone and mudstone facies in the Changhsingian and lower Griesbachian. The dominance of isorenieratane from the Meishan (Cao et al., 2009) and Shangsi (this paper) suggest that the water depths were deeper than 100 m, but estimates for the Shangsi outer ramp differ (Wignall et al., 1995). The Opal Creek section was deposited in an outer shelf setting (Schoepfer et al., 2013). The paleo-water depths
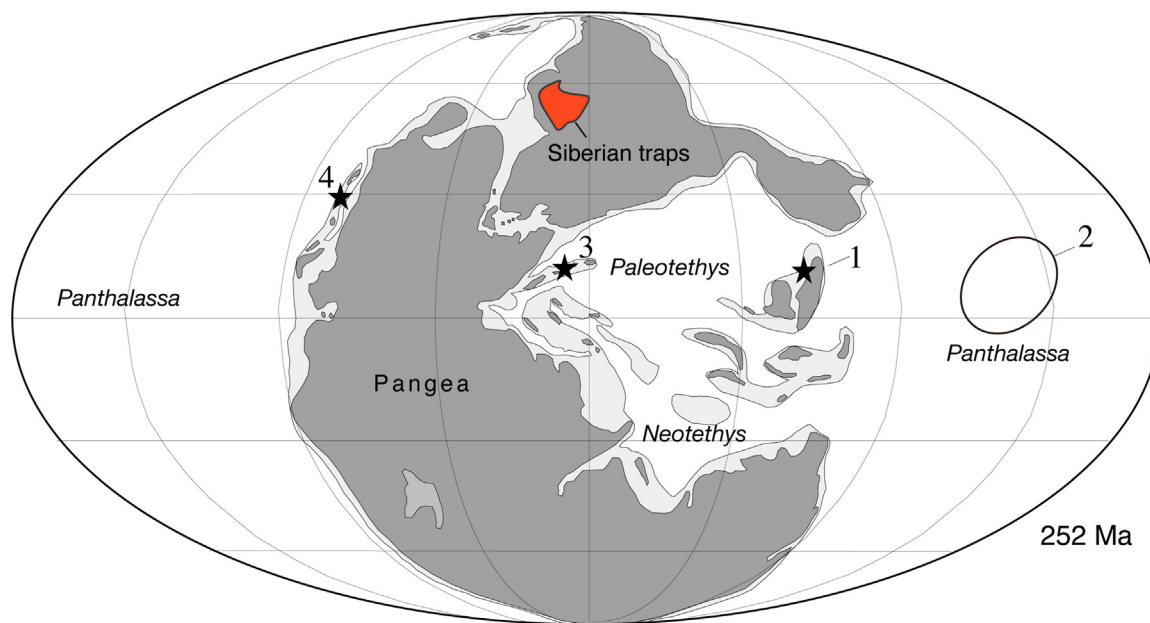
**Fig. 1.** Paleogeographic map showing the study sites and reference sections (Table 1). (1) multiple sections from South China (Dajiang, Huangzhishan, Bianzhonglu, Meishan, Shangsi), (2) multiple sections from Japan (Kamura, Akkamori, Ubara, Gujohachiman), (3) the Bulla section in Italy, and (4) the Opal Creek section in Canada. Also shown is the location of the Siberian Traps. The base map follows Ziegler et al. (1998).

at Ubara, Akkamori, and Gujohachiman were estimated to be ∼5000 m, based on ocean floor sediments of cherts and black shales. In these sections, the P/Tr extinction is marked by the demise of radiolarians.

## 2. Materials and methods

We used the C35 homohopane index, the ratios of gammacerane/C30 hopane (%) (gammacerane index), isorenieratane content, the pristane (Pr)/phytane (Ph) and dibenzofuran/phenanthrene (DBF/Phe) ratios, Mo/Al, U/Al, V/Al, and pyrite framboid size distribution to examine ocean redox conditions in 11 sections corresponding to the Changhsingian and Griesbachian (Fig. 1; Table 1). We also examined soil erosion states using DBF/Phe. To clarify the cause of oxygen depletion in the shallow seas, the upwelling (high productivity) proxy, extended tricyclic terpane ratios (ETRs), defined as (C28tricyclic terpane + C29tricyclic terpane)/Ts (C28TT + C29TT/Ts; Holba et al., 2001) at Bulla and Meishan were analyzed.

### 2.1. Biomarkers

We analyzed 30, 21, 23, 50, 19, 59, 70, and 18 samples from the Bulla, Dajiang, Kamura, Huangzhishan, Bianzhonglu, Meishan, Shangsi, and Ubara sections,

**Table 1.** Water depths, proxies, and data sources of the sections studied.

| Section | Country | Water depth (m) | Proxy | Source |
|---|---|---|---|---|
| Bulla | Italy | 10 | Pr/Ph, DBF/Phe, G/C30H, C35HI,(C28TT+C29) TT/Ts | Kaiho et al., 2012, This study |
| Dajiang | China | 30 | Pr/Ph, DBF/Phe | This study |
| Kamura | Japan | 30 | Pr/Ph, DBF/Phe | This study |
| Huanzhishan | China | 50 | Pr/Ph, DBF/Phe, G/C30H, C35HI | Kaiho et al., 2012 |
| Bianzhonglu | China | 50 | Pr/Ph, DBF/Phe, G/C30H, C35HI | This study |
| Meishan | China | 100 | Pr/Ph, DBF/Phe, G/C30H, C35HI,(C28TT+C29) TT/Ts | Kaiho et al., 2012, This study |
| Opal Creek | Canada | 100-300 | Mo/Al | Schoepfer et al., 2013 |
| Shangsi | China | 200-300 | Pr/Ph, DBF/Phe, G/C30H, C35HI | This study |
| Akkamori | Japan | 5000 | Mo/Al | Takahashi et al., 2014 |
| Gujohachiman | Japan | 5000 | Mo/Al, Pyrite[*] | Algeo et al., 2010, Wignall et al., 2010 |
| Ubara | Japan | 5000 | Pr/Ph, DBF/Phe, Mo/Al | This study |

[*] Small framboidal pyrites indicate intermediate water redox conditions.

respectively, for biomarkers according to the method of Kaiho et al. (2012). For each sample, hand-sized rock samples were crushed after removal of apparent surface contaminants by cutting and washing with dichloromethane/methanol (6:4, v/v). Powdered samples (100 g) were Soxhlet-extracted with dichloromethane/methanol (7:1, v/v) for 48 h. The extracts were dried over $Na_2SO_4$ and concentrated by evaporation under reduced pressure. The concentrated extracts were separated into four fractions on a silica gel column (0.6 g of silica, 63–200 μm) by elution using the following solvents: 2 ml of *n*-hexane (F1a); 4 ml of *n*-hexane (F1b); 3 ml of *n*-hexane/toluene 3:1 v/v (F2); and 1 ml of ethyl acetate and 10 ml of methanol (F3–8). Pr, Ph, C30 hopane, gammaceranes, C31–35 homohopanes, C28TT, C29TT, Ts, and Tm were recovered from the F1a fraction, and Phe and DBF were recovered from the F1b + F2 fraction. Identification of the hydrocarbons was performed on an Agilent 7890B GC equipped with an Agilent 7000 triple quadrupole mass spectrometer operated with an ionizing electron energy of 70 eV and scanned from m/z 50 to 550 with a scan time of 0.34 s. A fused silica HP-5MS capillary column (30 m, 0.25 mm i.d., 0.25 μm film thickness) was used, with helium as the carrier gas. Samples were injected at 50 °C and held at that temperature for 1.0 min; then the temperature was raised to 120 °C at a rate of 30 °C/min, to 310 °C at a rate of 5 °C/min, and finally held constant for 20 min. Multiple reaction monitoring (MRM) analyses for saturated hydrocarbons were performed using an Agilent 7890B GC equipped with an Agilent 7000 triple quadrupole mass spectrometer and HP-5MS capillary column (30 m, 0.25 mm internal diameter, 0.25 μm film thickness), using helium and nitrogen as the carrier

and collision gases, respectively. Samples were injected under the same configuration as in scan analysis.

Identification of Pr (m/z: 57), Ph (m/z: 57), Phe (m/z: 178), and DBF (m/z: 168) was based on comparisons of our mass spectra and retention time data to published data (Peters et al., 2005; Asif et al., 2009) and synthetic standards. Biomarkers such as C30 hopane, gammaceranes, C31–35 homohopanes, C28TT, C29TT, Ts, and Tm were obtained at each MRM transition based on published retention times and mass spectral peaks (Soldan and Cerqueira, 1986; Summons and Jahnke, 1990; Peters et al., 2005). The ratio of gammacerane to C30 hopane (gammacerane/C30H [%]) was calculated based on the peak areas (Fig. 2). Peak areas for both C22 epimers were used in the formula %C35 (22R + 22S)/(C31 + C32 + C34 + C35) (22R + 22S) to compute the C35 homohopane index (Peters et al., 2005).

DBF was not standardized against total organic carbon (TOC), which is commonly used for standardization, but instead against the amount of Phe to eliminate the effects of preservation of organic molecules. TOC is mostly composed of kerogen with a small amount of bitumen. The value of the ratio of bitumen to kerogen is dependent on the type of sample. Therefore, organic molecules should be standardized relative to a common organic molecule derived from multiple sources rather than a single one. Phenanthrene is a common and abundant organic molecule present in all sedimentary rocks. It is formed by the diagenesis (Wakeham et al., 1980) and combustion (Laflamme and Hites, 1978) of organic molecules derived
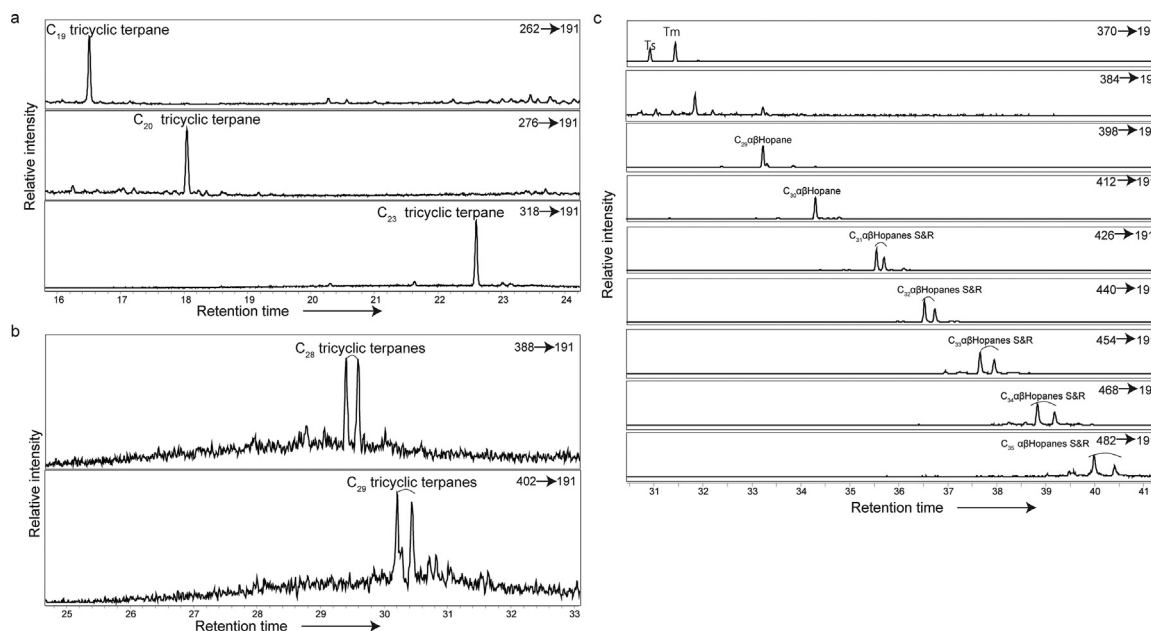


**Fig. 2.** GC-MSMS chromatograms showing tricyclic terpanes and hopanes for a sample in the Bulla section (BLA8 (0–3 cm)). a: C19, 20, 23 tricyclic terpanes. b: C28, 29 tricyclic terpanes. c: C27–35αβ-hopanes.

from the remains of organisms, and is derived not from a single source but from many sources (see refs in Nabbefeld et al., 2010). Moreover, DBF and Phe have similar rates of evaporation at a given temperature during the concentration process (Ahmed and George, 2004), but this is not the case for TOC. Therefore, it is preferable to use Phe for standardization rather than TOC.

## 2.2. Major and minor elements

Inorganic element analysis was performed on limestone, marlstone, and mudstone samples from the Huanzhishan, Bianzhonglu, and Shangsi sections using inductively coupled plasma–atomic emission spectrometry (ICP–AES; Thermo Scientific, iCAP6000 series). Mo, U, and V were analyzed using ICP mass spectrometry (ICP–MS; Perkin–Elmer, ELAN DRC II) after Takahashi et al. (2014). To allow comparisons of element enrichments, element concentrations are expressed as enrichment factors ($X_{EF}$; Tribovillard et al., 2006), in which sample concentrations are normalized to the average value of the upper continental crust (AUCC; McLennan, 2001):

$$X_{EF} = (Xsample/Alsample)/(X_{AUCC}/Al_{AUCC}), (1)$$

where X and Al are the weight concentrations of elements X and Al, respectively. Using this normalized enrichment factor, the fold-difference between the detected elemental concentration and the crustal material before erosion and sedimentation could be determined. The enrichment factors for Mo, U, and V ($Mo_{EF}$, $U_{EF}$, and $V_{EF}$) in the Ubara and Gujohachiman sections were those reported by Algeo et al. (2010).

## 2.3. Carbon isotopes

Stable isotope analyses of bulk powder were performed on limestone, marlstone, and mudstone samples from the Bianzhonglu section using a ThermoFisher DeltaV Advantage mass spectrometer, coupled with a ThermoQuest Kiel-III automated carbonate device. The $\delta^{13}C_{carb}$ and $\delta^{18}O$ values were calibrated to the NBS-19 international standard relative to VPDB. External precisions (1σ) for carbon isotope and oxygen isotope analyses, based on replicate measurements of a laboratory reference sample (JCt-1; Okai et al., 2004), were ±0.03‰ and ±0.05‰, respectively. For organic carbon isotopes ($\delta^{13}C_{org}$), all samples in the microcapsules were analyzed for the carbon stable isotope ratio using an elemental analyzer (CE Instruments Co. NA2500) linked to a mass spectrometer (Finnigan MAT Co. DELTA plus). Errors for replicate samples were within ±0.1‰. The carbon stable isotope ratios were expressed using the following equation: $\delta^{13}C$ (‰) = ($R_{sample}/R_{standard} - 1$) × 1000, where $R_{sample}$ is the $^{13}C/^{12}C$ of the sample and $R_{standard}$ is the $^{13}C/^{12}C$ of the standard, Pee-Dee Belemnite (PDB). For this

study, the $\delta^{13}C_{carb}$ values of the upper part of the Bulla section were measured using the method of Kaiho et al. (2012).

## 3. Results

All new data are shown in Supplementary Tables 1–8 (see the additional information).

### 3.1. Stratigraphic framework

Negative shifts in $\delta^{13}C_{carb}$ and $\delta^{13}C_{org}$ from the Bianzhonglu section coincided with the latest Permian extinction, from 4‰ to −2‰ and from −22‰ to −28‰, respectively (Fig. 3). Correlations among sections were based on new and previously published data on conodonts and stable carbon isotopes. Eight time horizons were chosen to examine the relationships among the representative sections (Fig. 3). $\delta^{13}C_{org}$ was used for the central Panthalassa because of its very low terrestrial organic matter content and the stable composition of source biota, except in extinction horizons, where the composition of the source biota may have changed. Level A was the minimum of $\delta^{13}C$ before the latest Permian extinction. Level B was the initiation of the highest plateau: ~4‰ for $\delta^{13}C_{carb}$ and ~−28‰ for $\delta^{13}C_{org}$. This level was dated to 63 kyr before the first decrease or the latest Permian extinction at the end of the Permian, according to the latest U/Pb dating of zircons from Meishan (Burgess et al., 2014). Level C was the end of the highest plateau. Level D was defined as ~2‰ for $\delta^{13}C_{carb}$ and −29‰ for $\delta^{13}C_{org}$. Level E contained the minimum values in the trough, with a $\delta^{13}C_{carb}$ of ~−2‰ and a $\delta^{13}C_{org}$ of −32‰. Level F was the highest value just before the second decrease: ~1‰ for $\delta^{13}C_{carb}$ and −30‰ for $\delta^{13}C_{org}$. Level G was the minimum value in the second trough, with a $\delta^{13}C_{carb}$ of ~−2‰ and a $\delta^{13}C_{org}$ of −33‰. Levels E and G corresponded to two episodes in the global carbon cycle reported by Xie et al. (2007b). Level H represented the recovery of $\delta^{13}C_{carb}$ to 2‰. Carbon isotope zones (CI zones) I–VI represented six time bins: between levels B and C, C and D, D and E, E and F, F and G, and G and H, respectively (Fig. 3).

### 3.2. Biomarkers and elements

Measurement of the above-described samples showed that 22S/(22S + 22R) $C_{31}$ homohopanes ranged from 0.57 to 0.59 in Bulla; were lacking in 22S and 22R, except for a single data point (0.54) in Dajiang; and were 0.49–0.63 in Kamura, 0.54–0.64 in Huangzhishan, 0.54–0.56 in Bianzhonglu, 0.55–0.62 in Meishan, 0.54–0.58 (single data point: 0.49) in Shangsi, and 0.57–0.60 in Ubara. These biomarker values indicate that all samples had reached maturity or surpassed the main phase of oil generation. Another diagenetic proxy, $\beta\beta/(\alpha\alpha + \beta\beta)$ C29 sterane, ranged from 0.42 to 0.56 in Bulla, 0.53 to 0.56 in Kamura, 0.44 to 0.66 in Huangzhishan, 0.50 to 0.59 (two samples were exceptionally low, 0.19 and 0.29) in
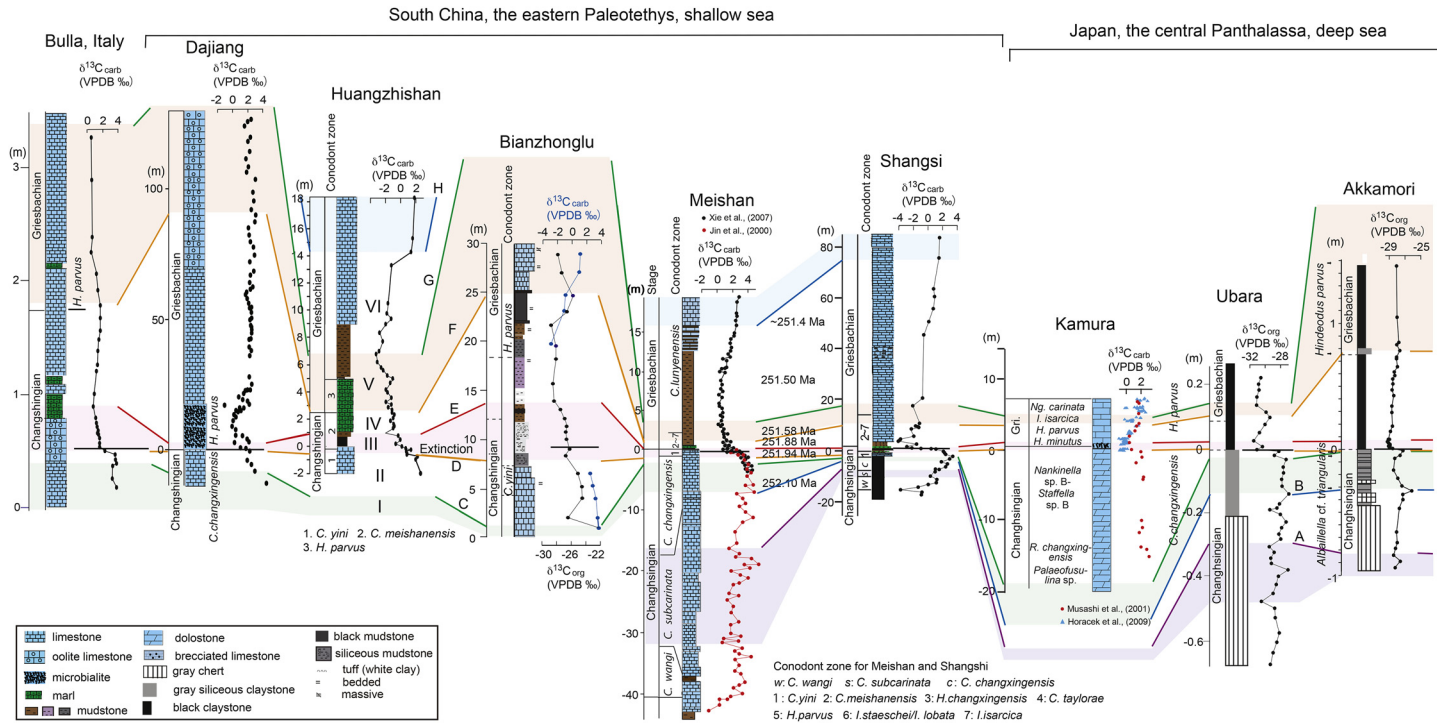
**Fig. 3.** Carbon isotope ratios spanning the Permian-Triassic mass extinction horizons in seven representative shallow sections in China, Italy, and Japan (carbonate carbon isotopes), and two representative deep-sea sections from Japan (organic carbon isotopes). The eight colored lines A–H represent carbon isotope events. The six colored areas I–VI, divided by the carbon isotope events, are carbon isotope zones. $\delta^{13}C$ data for the lower part of the Bulla section are after Gorjan et al. (2007), for Dajiang are after Payne et al. (2004), for Huangzhishan are after Chen et al. (2009), for Meishan are after Jin et al. (2000) and Xie et al. (2007), for Shangshi are after Riccardi et al. (2007) and Shen et al. (2013), for Kamura are after Musashi et al. (2001) and Horacek et al. (2009), for Ubara are after Kaiho et al. (2012), and for Akkamori are after Takahashi et al. (2010). Conodont data for Bulla are after Farabegoli et al. (2007), for Dajiang are after Yin et al. (2014), for Kamura are after Koike (1996), for Huangzhishan are after Chen et al. (2009), for Bianzhonglu are from unpublished data, for Meishan are after Yin et al. (2014) and Brosse et al. (2016), for Shangshi are after Yin et al. (2014), Chen et al. (2016), and Brosse et al. (2016), for Ubara are after Yamakita et al. (1999), and for Akkamori are after Takahashi et al. (2009). U/Pb dating of zircons from Meishan are after Burgess et al. (2014).

Bianzhonglu, 0.20 to 0.62 in Meishan, and 0.21 to 0.77 in Shangsi. These values indicate early to late stages of oil generation, but most samples belonged to the peak stage of oil generation (Peters et al., 2005).

In the Bulla section, the gammacerane and C35 homohopane indices had peaks (17 and 7) at 20–21 cm of Bed 8 corresponding to the latest Permian extinction (Fig. 4a). The values for the Pr/Ph ratio were high (2–3) in Beds 5 and 6, and low (0.8–1.3) in Bed 8. DBF/Phe values were high (0.1–0.3 for most samples) near the latest Permian extinction horizon, Beds 5 to 8. The values of the (C28TT + C29TT)/Ts ratio peaked four times and were >0.3 in CI Zones I–III in the Bulla section.

In the Dajiang section, the gammacerane and C35 homohopane indices and the values of the (C28TT + C29TT)/Ts ratio could not be evaluated because of the low contents of these molecules. Pr/Ph values were 0.8–1.5 in the Changhsingian and mostly 1.2–2.2 in the Griesbachian. DBF/Phe values were below 0.1, except a sample during the latest Permian extinction, CI Zone III (0.2; Fig. 4b).

There were few Hopanes in the Kamura section. Three gammacerane indices were calculated: the index was low in CI Zone II and high (4 and 3) in CI Zones III and IV (Fig. 4c). The C35 homohopane index and (C28TT + C29TT)/Ts ratio could not be evaluated because of the low contents of these molecules. Pr/Ph values were mainly low (0.4–0.8) throughout the section. The minima of the Pr/Ph values were detected in CI Zones III and IV. DBF/Phe values were high (0.2–0.4) between −0.55 m and −0.2 m and between −0.05 m and 0.22 m (Fig. 4c).

In Huangzhishan, the gammacerane and C35 homohopane indices had peaks (5 and 4) in the black mudstone in the latest Permian extinction horizon, CI Zone III (Fig. 4d). Pr/Ph values were mainly low (<1), except for horizons of high DBF/Phe. The DBF/Phe values were high (0.2–1.4) in the latest Permian extinction horizon, CI Zone III (Fig.   4d). $Mo_{EF}$, $U_{EF}$, and $V_{EF}$ values were low (0.01–0.10, 0.3–2.9, and 0.01–0.11, respectively) in CI Zone II and decreased significantly to <0.006, 0.03–0.25, and <0.01, respectively, in CI Zones III and IV (Fig. 4d).

In Bianzhonglu, DBF/Phe values were low (0.0002–0.06) throughout the respective sections (Fig. 4d). $Mo_{EF}$, $U_{EF}$, and $V_{EF}$ values decreased from high (>100, ~1000, ~80) to low (<10, <160, <11) in CI Zones II and III but reached high (~100, ~10, ~10) values in CI Zone V (Fig. 4e).

In the Meishan, the gammacerane and C35 homohopane indices showed decreasing trends but their values were high in CI Zone III (Fig. 4f). Isorenieratane was sometimes dominant in Zones I and II (Fig. 4f). DBF/Phe values were very high in CI Zone II–III (Fig. 4f). The (C28TT + C29TT)/Ts ratio peaked in CI Zone III.

In the Shangsi section, the gammacerane and C35 homohopane indices were low to high in CI Zones I–V and very high (30 and 8 at maximum) in CI Zone VI. This
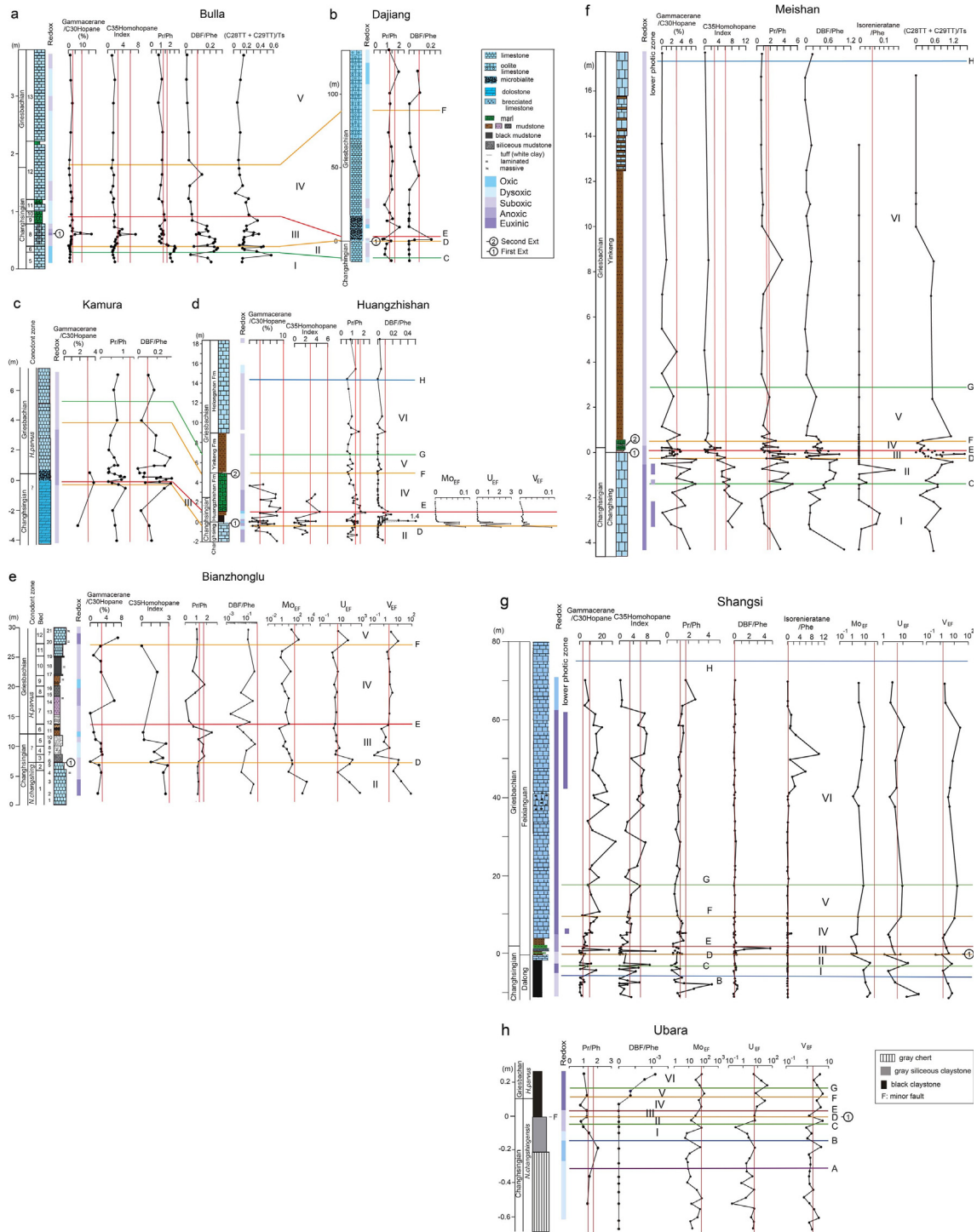
**Fig. 4.** Stratigraphic variation in hydrocarbon-derived paleoenvironmental parameters and atomic elements diagnostics for sedimentary redox conditions accompanied by hydrocarbon-derived geochemical parameters diagnostic for soil erosion (dibenzofuran/phenanthrene) and a marine productivity parameter ([C28TT + C29TT]/Ts) spanning the Permian–Triassic mass extinction at seven sections in Italy, South China, and Japan (Table 2). $Mo_{EF}$, $U_{EF}$, and $V_{EF}$ data in the Ubara section were calculated using the Mo, U, and V data of Algeo et al. (2010). a: Bulla. b: Dajiang. c: Kamura.

was a reversal of the trends in the shallower sections (Fig. 4g). DBF/Phe values were high (0.1–0.3) just below and during the latest Permian extinction (Fig. 4g). Isorenieratane appeared in the Griesbachian, in CI Zones IV–VI, and was extremely dominant in the upper part of CI Zone VI (isorenieratane/phenanthrene: 0.5/10). Intermediate $Mo_{EF}$, (6–21), high $U_{EF}$ (2–58), and high $V_{EF}$ (2–7) values in CI Zones I and II decreased to low values (1–3, 1–8, 1–3) in CI Zone III, then increased slightly (3–8, 3–10, 2–23) from CI Zone IV to Zone VI (Fig. 4e).

In the Ubara section, Pr/Ph values were high (1.3–2) from −0.6 to −0.1 m, and low (0.8–1.2) above these beds (Fig. 4h). DBF/Phe values were 0 in the Changhsingian and increased to 0.001 (very low) in the Griesbachian (Fig. 4h). $Mo_{EF}$, $U_{EF}$, and $V_{EF}$ values in the Ubara section were low in CI Zone I but gradually increased and were high in CI Zone VI (Fig. 4h).

## 4. Discussion

## 4.1. Redox proxies

The gammacerane and C35 homohopane indices, Pr/Ph coupled with DBF/Phe, the isorenieratane/Phe, framboid pyrite size, and the Mo, U, and V values were used to reconstruct paleoceanic redox conditions. These variables are defined in Table 2 and are based on the evidence and reasons described in the following. All of the values are approximate. The C35 homohopane index and Pr/Ph are redox proxies of surface sediments and depositional environment, whereas the gammacerane index and isorenieratane/Phe ratio are redox proxies of water. We found significant variation of the redox proxies of surface sediments corresponding to euxinic to oxic conditions (Fig. 5); therefore, these proxies should have reflected redox conditions in surface sediments and waters because redox conditions of subsurface fine-gained sediments would have been anoxic.

## 4.2. Pristane/phytane ratio as a redox proxy

The Pr/Ph ratio provides a measure of the redox conditions on the seafloor (Didyk et al., 1978; Killops and Killops, 2005; Sivan et al., 2008). However, it may be inaccurate as a redox proxy if the values are altered by diagenesis, which causes an increase in Pr/Ph, or if the source is not predominantly from chlorophyll (Rashid, 1979; Tang and Staauffer, 1995; Koopmans et al., 1999). The latter is the main source of Pr and Ph, but there are other sources, such as archaea,

---

d: Huangzhishan. e: Bianzhonglu. f: Meishan. g: Shangsi. h: Ubara. The marine extinction horizon at Bulla is after Gorjan et al. (2007). The two extinction horizons at Huangzhishan and Meishan are after Chen et al. (2009) and Song et al. (2013).

zooplankton, vitamin E (Goossens et al., 1984; De Rosa and Gambacorta, 1988; Rontani et al., 2013), land plants, and marine plans. In addition, soil intrusion of the sea can affect the reliability of Pr/Ph as a redox proxy.

Under relatively oxidizing conditions, a significant proportion of phytol can be oxidized into phytanic acid, which may then undergo decarboxylation into pristine before finally being reduced to pristane (Killops and Killops, 2005). In contrast, under relatively anoxic conditions, phytol is more likely to undergo reduction and dehydration into phytane via dihydrophytol (phytanol) or phytene. Because these chemical reactions do not depend on the geological age, we used the Pr/Ph ratio to reconstruct oceanic redox conditions.

The Pr/Ph boundary values defining each redox state vary and are not yet standardized. We compiled Pr/Ph data and evaluated the dissolved oxygen conditions as defined by other proxies; thus, anoxic conditions were defined as those in which Pr/Ph was <1.3 and oxic conditions were those in which Pr/Ph was >1.7 (Fig. 5a; Table 3). Intermediate values (1.3–1.7) were considered indicative of dysoxic conditions.

Pr/Ph ratios are also consistent with the appearance of isorenieratane, an excellent proxy for lower photic zone euxinia (Summons and Powell, 1987; Van Gemerden and Mas, 1995). Most samples in which isorenieratane/Phe ratios are >0.05 have Pr/Ph ratios < 1.3, whereas most samples in which Pr/Ph ratios are >1.3 have isorenieratane/Phe ratios > 0.05 at ~100 m water depth, which corresponds to the habitat water depths of green sulfur bacteria, the source of isorenieratane (Fig. 5b), and supports the definition of Pr/Ph.

The Pr/Ph ratios from recent and ancient sediments show a good correlation between Pr/Ph and redox conditions (Fig. 5a,Table 3). Specifically, Pr/Ph < 1.0 indicates anoxic and Pr/Ph > 1.0 indicates oxic conditions, based on data from recent sediments. Ancient Phanerozoic sediments influenced by diagenesis have a Pr/Ph < 1.3 when anoxic and a Pr/Ph > 1.7 when oxic. The difference in the Pr/Ph ratios between recent and ancient sediments is consistent with the effects of diagenesis because this process causes an increase in Pr/Ph ratios (Rashid, 1979; Tang and Staauffer, 1995; Koopmans et al., 1999).

The small coefficients of correlation (R-values) between the Pr/Ph and the $\beta\beta/(\alpha\alpha + \beta\beta)$C29 sterane maturity parameter in Bulla, Huangzhishan, Meishan, and Shangsi (Table 4) suggest that maturation had little influence on the Pr/Ph. All sections studied were of sufficiently high maturity, and any maturation effect had stabilized. This justified using Pr/Ph to reconstruct the redox conditions of the P/Tr oceans.

Following land invasion by plants in the Silurian and Devonian, an increase in soil erosion led to an increase in the Pr/Ph ratios because of the intrusion of pristane

**Table 2.** Criteria defining the different redox conditions.

| Redox condition | Dissolved oxygen (mL/L) | Gammacerane/ C30hopane (%) | C35homohopane index | Pr/Ph | Mo$_{EF}$ | U$_{EF}$ | V$_{EF}$ | Framboid pyrite size |
|---|---|---|---|---|---|---|---|---|
| Euxinic | 0 and presence of HS$^-$ | >10 | >6 | <1.3 | >80 | >6 | >2 | <5 μm |
| Anoxic | 0 | >3 | >3 | <1.3 | <80 | <6 | <2 | 5-6 μm? |
| Suboxic | 0–0.1 | <3 | <3 | <1.3 | <80 | <6 | <2 | 5-6 μm? |
| Dysoxic | 0.1–1.0 | <3 | <3 | 1.3-1.7[*] | <80 | <6 | <2 | 6-12 μm to no framboids? |
| Oxic | >1.0 | <3 | <3 | >1.7[*] | <80 | <6 | <2 | no framboids |

[*] DBF/Phe must be <0.1. Framboid pyrite size after Wilkin et al. (1996) and Wignall et al. (2010). Distinguishing among anoxic-suboxic, dysoxic, and oxic was difficult using framboid pyrite size; we could only classify conditions as euxinic or non-euxinic.

and phytane derived from land plants (e.g., high values in fluvial/deltaic environments; Hughes et al., 1995) and due to high inputs of terrestrial organic matter (Peters et al., 2005), which were produced in oxic conditions. Soil erosion can lead to increased Pr/Ph ratios because of the intrusion of Pr and Ph from land, where these compounds are usually oxidized. When the soil erosion proxy DBF/Phe is high, Pr/Ph is thought to be influenced by soil erosion. This is likely a reason for the lack of a single definitive indicator of oceanic redox conditions for Pr/Ph (Didyk et al., 1978). In our study, when Pr/Ph was >1.3, the DBF/Phe ratios in nearshore sections (Huangzhishan and Meishan) were between 0.1 and 1.0 during and around the time of the latest Permian extinction (Figs. 4d,f). Therefore, we suggest that Pr/Ph values are influenced by soil erosion when DBF/Phe is >0.1. However, the Pr/Ph ratio is reliable when Pr/Ph is <1.3.

If the contribution of archea to the sum of Pr and Ph is >60% then Pr/Ph will increase from 1.3 (the maximum value of Pr/Ph for anoxic conditions) to 1.7 (the minimum value of Pr/Ph for oxic conditions). An archaeal contribution of that size is rare because, based on fossil records, photosynthetic bacteria and eukaryotes (i.e., stromatolites, acritarchs, and multicellular algae) thrived during these ages. The contributions of zooplankton and vitamin E were minimal and thus had less influence than bacteria and eukaryotic algae on the Pr/Ph ratio.

## 4.3. Isorenieratane

Isorenieratane is derived from photosynthetic green sulfur bacteria (Summons and Powell, 1987). Chlorobiaceae are phototrophic anaerobes and require both light and H$_2$S for growth. In modern environments, they appear in sulfate-containing water bodies that are sufficiently quiescent and organic-rich to enable sulfide
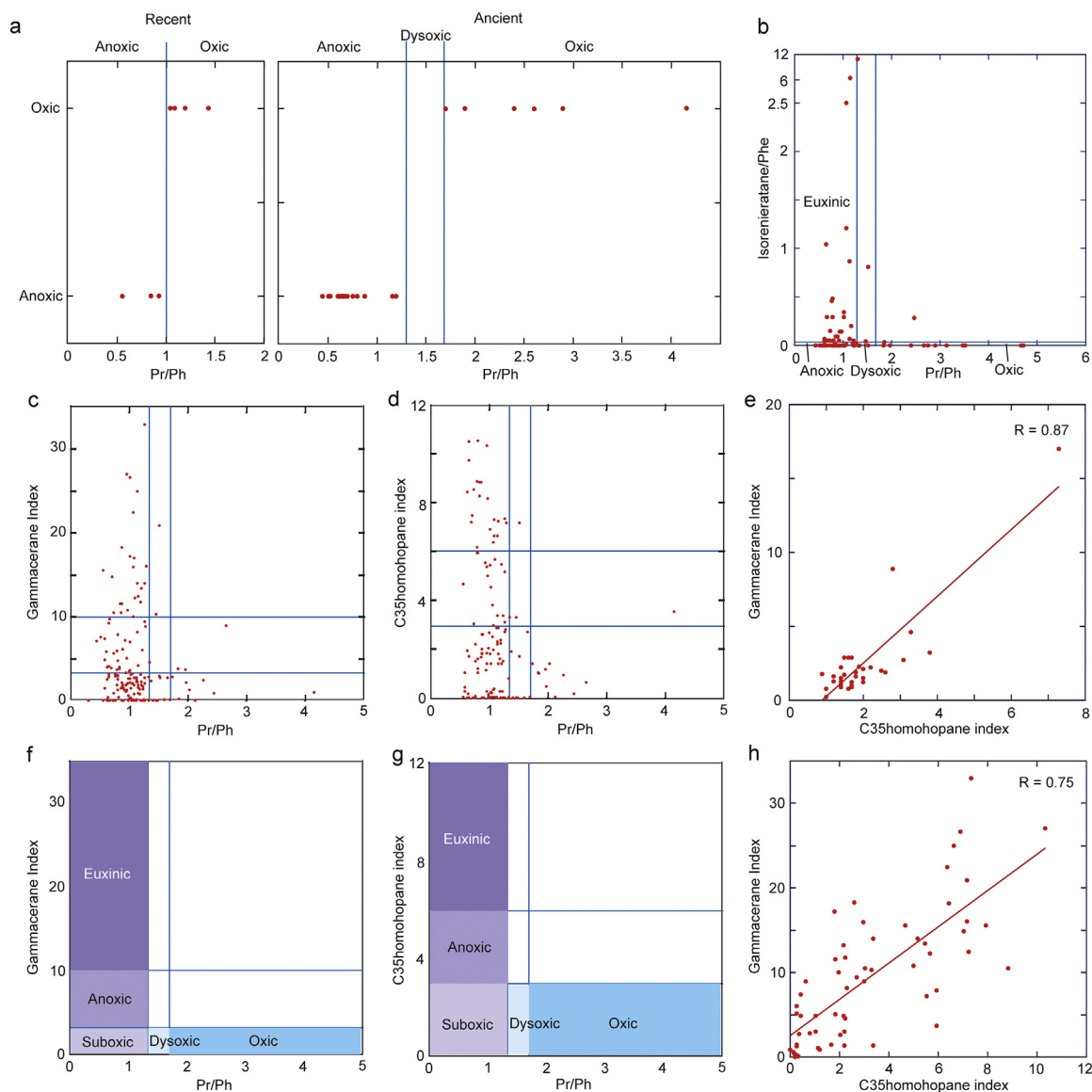
Fig. 5. Relationship between hydrocarbon-derived geochemical parameters diagnostic for sedimentary redox conditions and redox conditions. a: Pr/Ph and redox conditions after Table 2 (Didyk et al., 1978; Kaiho et al., 2012). b: Pr/Ph and isorenieratane/Phe in the Meishan and Shangsi sections, South China. c: Pr/Ph and the gammacerane index in all sections. d: Pr/Ph and the C35 homohopane index in all sections. For c and d, Pr/Ph from samples with DBF/Phe > 0.1 were neglected when Pr/Ph > 1.3. e: Gammacerane and C35 homohopane indices in Bulla. f: Definition of the redox conditions with respect to Pr/Ph and the gammacerane index. g: Definition of the redox conditions with respect to the Pr/Ph and the C35 homohopane index. h: The gammacerane and C35 homohopane indices in Shangsi.

production close to the photic zone (Summons, 1993). The occurrence of isorenieratane within sedimentary rocks is interpreted as the establishment of euxinic conditions in the lower part of the photic zone.

**Table 3.** Data on the pristane/phytane ratios and oceanic dissolved oxygen conditions.

| Pr/Ph | Oxicity/anoxi city | Sediments | Age | Depositional environment | Place | Sample No. |
|-------|--------------------|-----------|-----|--------------------------|-------|------------|
| 0.93 | Anoxic | Recent | 2 Ka | Marine | Cariaco Trench | 147B-1-1 (2) |
| 0.54 | Anoxic | Recent | 5 Ka | Marine | Cariaco Trench | 147B-1-3 (4) |
| 0.85 | Anoxic | Recent | 3 Ka | Marine | Black Sea | 1461K (0.4) |
| 1.04 | Oxic | Recent | 14 Ka | Lacustrine | Black Sea | 1462 (2.95) |
| 1.09 | Oxic | Recent | 16.5 Ka | Lacustrine | Black Sea | 1462 (5.0) |
| 1.43 | Oxic | Recent | 20 Ka | Lacustrine | Black Sea | 1474 (8.55) |
| 1.20 | Oxic | Recent | 22.8 Ka | Lacustrine | Black Sea | 1474 (11.55) |
| 0.56 | Anoxic | Ancient sediments | Eocene | Lacustrine | Green River Formation Oil Shale | |
| 0.68 | Anoxic | Ancient sediments | Eocene | Lacustrine | Messel Shale | |
| 0.45 | Anoxic | Ancient sediments | Cretaceous | Marine | La Luna Shale (Mara Outcrop) | |
| 0.55 | Anoxic | Ancient sediments | Cretaceous | Marine | La Luna Shale (36-2, 5,000 m) | |
| 0.50 | Anoxic | Petroleums | Eocene[*] | Marine | Boscan Credu 8E4 | |
| 0.50 | Anoxic | Petroleums | Eocene[*] | Marine | Boscan Credu BN4 | |
| 0.66 | Anoxic | Petroleums | Cretaceous | Marine | La Paz Crude P187 | |
| 0.70 | Anoxic | Petroleums | Cretaceous | Marine | Burgan Crude (Kuwait) | |
| 1.20 | Anoxic | Petroleums | Miocene | Marine | Wilmington Crude (USA) | |
| 2.40 | Oxic | Ancient sediments | Jurassic | Marine | Posidonia Shale | |
| 1.90 | Oxic | Petroleums | Cretaceous | Deltaic | Daniel Crude (Chile) | |
| 2.90 | Oxic | Petroleums | Cretaceous | Deltaic | Dicky Crude (Chile) | |
| 0.52 | Anoxic[**] | Ancient sediments | late Permian | Marine | Meishan | CHMI-1400 |
| 0.62 | Anoxic[**] | Ancient sediments | late Permian | Marine | Meishan | CHMI-1530 |
| 0.44 | Anoxic[**] | Ancient sediments | late Permian | Marine | Meishan | CHMI-2050 |
| 0.84 | Anoxic[**] | Ancient sediments | late Permian | Marine | Meishan | CHMI-2256 |
| 0.65 | Anoxic[**] | Ancient sediments | late Permian | Marine | Meishan | CHMI-2350 |
| 0.67 | Anoxic[**] | Ancient sediments | late Permian | Marine | Meishan | CHMI-2350 |
| 0.76 | Anoxic[**] | Ancient sediments | late Permian | Marine | Meishan | CHMI-2470 |
| 0.61 | Anoxic[**] | Ancient sediments | late Permian | Marine | Meishan | CHMI-2700 |
| 0.63 | Anoxic[**] | Ancient sediments | late Permian | Marine | Meishan | CHMI-2988 |
| 1.16 | Anoxic[**] | Ancient sediments | late Permian | Marine | Meishan | CHMI-3000 |
| 0.65 | Anoxic[**] | Ancient sediments | late Permian | Marine | Meishan | CHMI-3200 |
| 0.96 | Anoxic[**] | Ancient sediments | late Permian | Marine | Meishan | CHMI-3476 |
| 1.31 | Anoxic[**] | Ancient sediments | late Permian | Marine | Meishan | CHMI-1400 |
| 4.15 | Oxic[***] | Ancient sediments | late Permian | Marine | Meishan | CHMI-4460 |
| 1.72 | Oxic[***] | Ancient sediments | Early Triassic | Marine | Shangsi | CNSS115 |
| 2.66 | Oxic[***] | Ancient sediments | Early Triassic | Marine | Shangsi | CNSS114 |

Data from Meishan and Shangsi after this paper. The other data are after Didyk (1978).

[*] Age of reservoir rock.

[**] Isorenieratane/Phe: >0.05 at a paleowater depth of about 100 m. Data after Kaiho et al. (2012).

[***] Isorenieratane/Phe: 0 at a paleowater depth of about 100 m. Gammacerane/C30hopane (%) <3, C35homohopane index <3.

## 4.4. Gammacerane and C35 homohopane indices

The small coefficients of correlation (R-values) between the C35 homohopane index or gammacerane index and the $\beta\beta/(\alpha\alpha + \beta\beta)$C29 sterane maturity parameter in Bulla, Huangzhishan, and Shangsi (Table 4) suggest that maturation had little influence on the C35 homohopane and gammacerane indices. The C35 homohopane index of Meishan and the C35 homohopane and gammacerane indices of Bianzhonglu should be used with caution because of the intermediate correlations (Table 4). However, excluding them did not influence our conclusions regarding the redox conditions in Meishan and Bianzhonglu (Fig. 4).

As the influence of biodegradation on the C35 homohopane index likely occurs after the severe biodegradation stage (i.e., production of 25-norhopane) (Peters and Moldowan, 1991; Peters et al., 2005), this index was likely not affected by biodegradation in our samples; the presence of short-chain n-alkane indicated the absence of severe biodegradation.

To our knowledge, temperature does not affect the gammacerane index. Salinity affects this index indirectly, and reducing conditions affect it directly. Gammacerane is derived from ciliates that feed on green sulfur bacteria (Sinninghe Damsté et al., 1995), which are anoxic photosynthesizers (Summons and Powell, 1987). Because green sulfur bacteria inhabit lakes with stratified water columns in modern settings and ciliates feed on them, the presence of gammacerane is thought to be an indicator of a stratified water column (Sinninghe Damsté et al., 1995). In addition, organisms with genes producing a precursor of gammacerane live in oxygen-poor environments (Takishita et al., 2012). These lines of evidence indicate that gammacerane is a good indicator of reducing conditions of bottom water to the overlying water column, and salinity is an indirect factor affecting redox conditions. Gammacerane has been related to hypersalinity (Peters and Moldowan, 1991), which in turn suggests water column stratification and bottom-water anoxia (Sinninghe Damsté et al., 1995). The C35 homohopane index is mainly used to detect the redox condition of the depositional setting (Peters and Moldowan, 1991). Although it is a good proxy for ocean redox, there are no validated definitions of anoxic-suboxic or oxic conditions (Kasprak et al., 2015). The gammacerane and C35 homohopane indices showed a good correlation in the sections studied (Fig. 4, Figs. 5e, h), implying that the gammacerane index can also be used as an anoxic indicator. Based on the relationships among isorenieratane/ Phe and Pr/Ph (Fig. 5b), the gammacerane index and Pr/Ph (Fig. 5c), the C35 homohopane index and Pr/Ph (Fig. 5d), and the good correlation between the gammacerane and C35 homohopane indices (Figs. 5e, h), the redox conditions could be defined. Thus, the redox conditions were euxinic at a gammacerane index > 10 or a C35 homohopane index > 6 and a Pr/Ph ratio < 1.3; anoxic at a gammacerane or C35 homohopane index > 3 and a Pr/Ph ratio < 1.3; suboxic at a

**Table 4.** Coefficients of correlation R (CCR) between the gammacerane index (GI) and the maturity parameter, ββ/(αα+ββ) C29 sterane, between the C35 homohopane index (C35HHI) and the maturity parameter, and between pristine/phytane and the maturity parameter in studied sections.

| Section | CCR between GI and maturity index | CCR between C35HHI and maturity index | CCR between Pr/Ph and maturity index | No. samples for maturity index | No. samples for gammacerane index | No. samples for C35HHI | No. samples for Pr/Ph |
|---|---|---|---|---|---|---|---|
| Bulla | -0.08 | -0.04 | -0.02 | 32 | 32 | 32 | 30 |
| Huangzhishan | -0.08 | +0.20 | +0.21 | 21 | 30 | 29 | 54 |
| Bianzhonglu | +0.41 | +0.48 | -0.79 (-0.30[*]) | 12 | 15 | 10 | 19 |
| Meishan | +0.21 | +0.59 | -0.44 | 40 | 46 | 34 | 100 |
| Shangsi | -0.13 | +0.12 | +0.01 | 17 | 64 | 63 | 69 |

The original data are shown in the Supplementary Tables (Kaiho et al. 2016 SI).

[*] one sample neglected.

gammacerane or C35 homohopane index < 3, or in the absence of data indicating little gammacerane and C35 homohopane, and a Pr/Ph < 1.3; dysoxic at a gammacerane or C35 homohopane index < 3, or in the absence of data, and a Pr/Ph of 1.3–1.7; and oxic at a gammacerane or C35 homohopane index < 3, or in the absence of data, and a Pr/Ph > 1.7 (Figs. 5f, g; Table 2).

## 4.5. Molybdenum, uranium, and vanadium

The elements Mo, U, and V tend to be authigenically enriched in sediments under reducing conditions (Algeo and Maynard, 2004; Tribovillard et al., 2006). We used the calculated enrichment factors ($Mo_{EF}$, $U_{EF}$, $V_{EF}$) of these elements ($Mo_{EF}$-$U_{EF}$ method). When $Mo_{EF} > 80$, $U_{EF} > 6$, and $V_{EF} > 2$, the redox conditions were euxinic, following a previous study (minimum values of sapropels and Cenomanian/Turonian black shales after Brumsack, 2006; Table 2). In the deep sea, these proxies are thought to indicate the respective redox conditions because Mo, U, and V mostly precipitate at the sediment–water interface (Algeo et al., 2010). However, values of $Mo_{EF}$, $U_{EF}$, and $V_{EF}$ during and after the latest Permian extinction cannot be used as straightforward redox indicators because of the drawdown of these trace elements from the global ocean (Takahashi et al., 2014).

## 4.6. Framboidal pyrite

Abundant small (<5 μm) framboids of pyrites and a narrow size distribution indicate euxinic conditions in the water column (e.g., Wilkin et al., 1996). These framboids precipitate in the sulfidic water column, while large pyrite framboids form at the sediment–water interface (Wilkin et al., 1996; Wilkin and Barnes, 1997; Wignall and Newton, 1998; Wignall et al., 2010; Tian et al., 2014). The

redox conditions of intermediate waters were estimated using the framboids from the deep-sea sedimentary rocks (Table 2).

## 4.7. Iron speciation

Xiang et al. (2016) extracted the mass fractions of carbonate-associated iron phases ($Fe_{carb}$), iron oxides ($Fe_{ox}$), magnetite-associated iron phases ($Fe_{mag}$), and pyrite iron ($Fe_{py}$) to estimate dissolved oxygen conditions spanning the latest Permian extinction. Soil erosion can lead to increased levels of iron oxides in marine water because of their intrusion from land, where iron is usually oxidized. However, we did not use iron speciation data to estimate the dissolved oxygen conditions characterizing the soil erosion event that occurred during the latest Permian extinction.

## 4.8. Redox conditions in each section

The redox conditions of water at the sediment surface in the 11 sections (Table 1) were estimated using new and published organic molecule proxy data, redox-sensitive elements, and the small framboid size distribution (Fig. 4), based on the above-defined redox conditions. As each sample was 1–10 cm in thickness, the resulting data represent the average fluctuations in the redox conditions at the time of specimen deposition.

The redox conditions of the water at the sediment surface on carbonate facies on the inner shelf in the western margin of the Paleotethys (Bulla) were oxic CI Zones I and II, based on the low gammacerane (<3) and C35 homohopane (<3) indices and the high Pr/Ph (>1.3); the ratio could be used because of the low DBF/Phe (<0.1) of the two samples (Fig. 4a). The high gammacerane (>3 or >10) and C35 homohopane (>3 or >6) indices indicated short-term anoxic–euxinic conditions in CI Zone III, coinciding with the culmination of extinction. The low gammacerane (%) and C35 homohopane indices and the low to intermediate Pr/Ph with a low DBF/Phe suggested dysoxic conditions in CI Zones IV and V. The dominance of small pyrites (4–6 µm) at the base of Bed 8 (Gorjan et al., 2007) also evidenced the euxinic–anoxic conditions in CI Zone III.

In Dajiang, an intermediate Pr/Ph with a low DBF/Phe value was detected in CI Zone I, indicating that the redox conditions of the water at the sediment surface on carbonate facies on the inner shelf in the eastern margin of the Paleotethys were dysoxic in CI Zone I (Fig. 4b). Suboxic conditions in CI Zone II were indicated by the low (<1.3) to intermediate (1.3–1.7) Pr/Ph with low DBF/Phe values. In CI Zone III, the low Pr/Ph indicated suboxic conditions. In CI Zones IV and V, the intermediate Pr/Ph with low DBF/Phe values indicated dysoxic conditions.

The Panthalassic carbonate seamount in Kamura was deposited under dysoxic conditions in CI Zone II, based on the intermediate gammacerane index (2) and low Pr/Ph (0.7–1.1; Fig. 4c). A high gammacerane index (>3) and very low Pr/Ph (<0.7) in CI Zones III and IV indicated anoxic conditions. CI Zones V and VI were estimated to be dysoxic, based on the low Pr/Ph, with values similar to those in CI Zone II.

The middle-shelf carbonate facies with mudstone at Huangzhishan was deposited under anoxic and then dysoxic conditions in CI Zone II, based on the high gammacerane index and intermediate C35 homohopane index (>2) followed by low gammacerane and C35 homohopane indices (<2), an intermediate Pr/Ph with a low DBF/Phe, and low $Mo_{EF}$, $U_{EF}$, and $V_{EF}$ values (Fig. 4d). The high gammacerane and C35 homohopane indices in the black mudstones indicated anoxic conditions in CI Zone III, a finding strengthened by the presence of abundant pyrite framboids (Chen et al., 2009). The high gammacerane and C35 homohopane indices in CI Zone IV indicated anoxic conditions. Suboxic conditions in CI Zones V and VI were suggested by the low Pr/Ph, with a low DBF/Phe, and the absence of gammacerane and C35 homohopane. The significant decreases in $Mo_{EF}$, $U_{EF}$, and $V_{EF}$ in CI Zone III despite evidence of organic molecules indicating anoxic condition were likely due to the drawdown of these trace elements from the regional water mass corresponding to the Huangzhishan or the global oceanic inventory estimated from the significant accumulation of these elements in CI Zone III in Akkamori (Takahashi et al., 2014).

The redox conditions in Bianzhonglu were euxinic in CI Zone II, as indicated by the high $Mo_{EF}$, $U_{EF}$, and $V_{EF}$ values (near 2.5; Fig. 4e). In CI Zone III, the intermediate Pr/Ph, with a DBF/Phe <0.1, indicated dysoxic conditions. In CI Zone IV, the low Pr/Ph ratio suggested mostly suboxic conditions. Intermediate $Mo_{EF}$, high $U_{EF}$, and high $V_{EF}$ values supported by a high gammacerane index indicated euxinia in CI Zone V.

The carbonate facies with mudstone on the middle to outer shelf in Meishan was euxinic to anoxic in CI Zone I, and anoxic in CI Zones II and III, based on the gammacerane index (Fig. 4f). The low gammacerane index and Pr/Ph ratio indicated suboxic to dysoxic conditions in CI Zone IV–VI. An isorenieratane/Phe ratio >0.05 in CI Zones I and II indicated that euxinic conditions sometimes developed in the lower part of the photic zone (80–100 m) in Changshingian in the Meishan. Although Grice et al. (2005) and Cao et al. (2009) reported isorenieratane in the latest Permian extinction horizon, we found no evidence of this compound. The estimated paleowater depths were around 100 m, similar to the depth of the lower photic zone.

In a previous study, the $Mo_{EF}$, $U_{EF}$, and $V_{EF}$ values at Opal Creek were ~10, ~2, and ~2, respectively, in CI Zones II and III, and <10, ~2, and 1–2 in CI Zones

IV–VI (Schoepfer et al., 2013), indicating that the redox conditions in the eastern Panthalassic outer shelf were not euxinic and likely suboxic in CI Zones II and III. The redox condition of CI Zones IV–VI could not be determined because of the drawdown of these trace elements.

Mudstone facies on the outer shelf to upper slope in Shangsi were deposited under anoxic conditions in CI Zone I (Fig. 4g). Suboxic conditions in CI Zone II followed anoxic conditions in CI Zone III. The euxinic conditions extended to CI Zones IV–VI. Isorenieratane appeared in the Changhsingian, including CI Zones I and II, in Meishan, and in the Griesbachian in CI Zones IV and VI in Shangsi (~6 m and ~18–62 m; Supplementary Table 7). The abundance of isorenieratane/ phenanthrene was 10 times higher there than in Meishan, indicating its extreme dominance in the late Griesbachian. Euxinic conditions developed in the lower part of the photic zone (80–100 m) in the Griesbachian and in an extremely high in the late Griesbachian. This coincided with an increase in surface water temperature during the Griesbachian, with maxima reached in the *Is. isarcica* and *Ng. planata* zones, CI Zones V and VI (Joachimski et al., 2012; Sun et al., 2012). The significant decrease in $Mo_{EF}$, $U_{EF}$, and $V_{EF}$ in CI Zone III may have been due to the drawdown of these trace elements from the global oceanic inventory (Takahashi et al., 2014). Dissolved oxygen conditions spanning the latest Permian extinction, as estimated by iron speciation in Shangsi (Xiang et al., 2016), were similar to those determined from sedimentary organic molecules in Meishan and Shangsi, except in CI Zone III (Figs. 4f, g). The discrepancy can be explained by a massive soil erosion event (Sephton et al., 2005; Nabbefeld et al., 2010; this study) that led to increased iron oxides because of their intrusion from land, where iron is usually oxidized.

In Akkamori, the $Mo_{EF}$, $U_{EF}$, and $V_{EF}$ values (Takahashi et al., 2014) rose from the late Changhsingian siliceous claystone beds toward the basal 2 cm of black claystone corresponding to the latest Permian extinction event, suggesting euxinic conditions. A significant decrease in $Mo_{EF}$, $U_{EF}$, and $V_{EF}$ also occurred in the deep water just after the latest Permian extinction, which could have been due to the drawdown of these trace elements from the global oceanic inventory (Takahashi et al., 2014).

In Ubara, the Pr/Ph was used to reconstruct the redox conditions, which was possible because of the very low DBF/Phe. Dysoxic conditions in CI Zone I became suboxic in CI Zone II, as suggested by the Pr/Ph values; low $Mo_{EF}$, $U_{EF}$, and $V_{EF}$; and presence of pyrite framboids (Algeo et al., 2010; Algeo et al., 2011; Fig. 4h). In CI Zones III and IV, increases in $Mo_{EF}$, $U_{EF}$, and $V_{EF}$ and a further decrease in Pr/Ph were determined, indicating the continued development of reduced conditions. The high $Mo_{EF}$, $U_{EF}$, and $V_{EF}$ values indicated euxinic conditions in CI Zones IV–VI. The strong euxinic trend of a much higher $Mo_{EF}$

and $V_{EF}$ observed in the Akkamori section was not detected in the Ubara section. This difference may be due to the lack of a stratigraphic layer corresponding to the latest Permian extinction because of a minor fault, as reported by Tada et al. (2005), and spatial variation in the flux of buried organic matter similar to that proposed by Algeo et al. (2011).

In Gujohachiman, the variation in trace elements was similar to that in the Ubara section (Algeo et al., 2011). Low Mo, U, and V contents in the horizons in CI Zone I increased in CI Zone II. Although Algeo et al. (2011) interpreted this increase as evidence of suboxic conditions because the respective values were not particularly high, the trace elemental drawdown proposed by Takahashi et al. (2014) would suggest the need for a re-interpretation using multi redox proxies such as organic molecules.

The pyrite morphology in the Ubara and Gujohachiman sections indicated the absence of a euxinic water column in CI Zone I, and euxinic conditions in CI Zones II–V in water of intermediate depth (Wignall et al., 2010; Algeo et al., 2011).

A combination of deep-water euxinia, evidenced by high values of $Mo_{EF}$, $U_{EF}$, and $V_{EF}$ in CI Zones II–IV in the Akkamori, and euxinia in CI Zones V and VI in the Akkamori and Ubara accompanied by a low Pr/Ph in the Ubara indicated that the dysoxic redox conditions in the central pelagic deep-sea Panthalassa in CI Zone I had changed to euxinic conditions in CI Zones II–VI.

## 4.9. Ocean redox structure

The above redox proxy values from six sections representative of shallow surface, deep surface, and intermediate waters in the Paleotethyan Ocean and five sections representative of shallow surface, intermediate, and deep waters in the Panthalassic Ocean and spanning the P/Tr mass extinction provide a new scheme of ocean redox structure.

Although data for deep water (>1000 m depth) are only available for the Panthalassic Ocean, compilation of the redox ocean structure in the Panthalassic Ocean and Paleotethyan Ocean showed: (1) dysoxic deep water with anoxic to non-euxinic intermediate water, euxinic deep surface water, and dysoxic to oxic shallow surface water, indicating that oceanic oxia in CI Zone I had changed to yield euxinic to suboxic deep and intermediate waters, anoxic-suboxic deep surface water, and suboxic to oxic shallow nearshore bottom water in CI Zone II, consistent with oceanic anoxia; (2) euxinic–suboxic conditions in the shallow nearshore bottom water occurred in CI Zone III; and (3) partial recovery of the surface water and culmination of anoxia–euxinia in the intermediate water in CI Zone IV (Fig. 6).

Intermediate water in CI Zone I corresponded to the OMZ in the oxygenated ocean (oceanic oxia; Fig. 6). Intensification of the OMZ, anoxic-euxinic conditions, occurred in CI Zone II. The expansion of the OMZ to the deep surface water occurred in CI Zone III. Suboxic conditions occurred in the nearshore bottom waters, accompanied by a short-term anoxic–euxinic bottom water in CI Zone III. The anoxic conditions in the surface sediment and bottom water occurred only at the latest Permian extinction, persisting for only a short time on the order of a thousand years or less, but not at the earliest Triassic extinction (Fig. 7).

The euxinic conditions in the intermediate water continued in CI Zones IV to VI, however, the surface water recovered and became suboxic to dysoxic. In deep water, dysoxic conditions gradually changed to euxinic ones in CI Zones I–IV until Zone VI. The long-term euxinic conditions coincided with an increase in surface water temperature, estimated using conodont apatite $\delta^{18}O$ in the Paleotethys (Sun et al., 2012). The extremely high concentration of isorenieratane at the Shangsi in CI Zone VI implied that the extreme warming led to the proliferation of green sulfur bacteria in the late Griesbachian.

## 4.10. Massive soil erosion followed by high productivity

A soil erosion event that occurred at the end-Permian extinction has already been reported (Sephton et al., 2005; Nabbefeld et al., 2010). However, these records are restricted to a few nearshore sequences. An organic molecule soil-erosion proxy, the DBF/Phe ratio (Kaiho et al., 2013), peaked at values >0.1 during the latest Permian extinction throughout the inner continental shelf to the upper continental slope, at an isolated platform in the Paleotethys, and at a seamount in the central Panthalassic Ocean; in contrast, no peaks were seen at a slope of the isolated platform in the Paleotethys and in the deep Panthalassic Ocean (Fig. 8). Furthermore, we found high DBF/Phe ratios (0.3–1.4) throughout the inner continental shelf to the upper slope and a seamount, and low values at the isolated platform (0.2), its slope (0.06), and in the central deep ocean (0.00) in CI Zone III. This water depth gradient pattern indicated that a destruction of the land vegetation should have occurred, leading to massive soil erosion and the massive transport of soils from land to the sea during the end-Permian extinction. This event may have given rise to an influx of mud as well as to ocean fertilization and intermittent oxygen-depleted surface water.

The highest DBF/Phe values in the top 4 cm of Bed 24, followed by the highest upwelling and productivity represented by the highest (C28TT + C29TT)/Ts values occurred during 3 to 6 kyr in CI Zone III at Meishan (22 cm/60 kyr between Bed 24 and 28 based on Burgess et al., 2014; Fig. 7). In Bulla, which had a higher resolution and the shallowest section, the highest DBF/Phe values occurred in the basal 19 cm of Bed 8 and were followed by a maximum in the (C28TT + C29TT)/

Ts ratio that coincided with the peaks of the gammacerane and C35 homohopane indices at 20–21 cm of Bed 8 during 2.1 kyr (based on 120 cm/50 kyr; Rampino et al., 2002) or 2.5 kyr (based on 120 cm/60 kyr; Burgess et al., 2014) in CI Zone III. The (C28TT + C29TT)/Ts ratio profile and the DBF/Phe ratio showed roughly mirror symmetry at Meishan and Bulla, suggesting that muddy opaque seawater developed near the coast, followed by transparent seawater dominated by nutrients, resulting in high primary productivity, algal blooms, and oxygen-depleted water during the latest Permian extinction. The lag between the erosion and the bloom is 4 kyr.

Increased marine productivity and successive enhanced microbial sulfate reduction events could have occurred on the shelf at the latest Permian extinction event (Schobben et al., 2014; Schobben et al., 2015). We propose here that the soil and rock erosion event induced high marine productivity and intermittent anoxic-–euxinic conditions in nearshore surface waters.

## 4.11. Limitations of bioessential elements

An abrupt and long-lasting decrease in bulk-rock U content coincided with the carbon isotope shift and the latest Permian extinction in the carbonates of the Khuff Formation in the Persian Gulf, north of Qatar (Ehrenberg et al., 2008). In addition, decreases in the values of $Mo_{EF}$, $U_{EF}$, and $V_{EF}$ were detected in CI Zones III and IV in Huangzhishan (shallow surface water, this study), Bianzhonglu (deep surface water, this study), and Shangsi (shallow intermediate water; Xiang et al., 2016; this study), and in CI Zones IV and V in the Akkamori (deep water; Takahashi et al., 2014). For example, $Mo_{EF}$ was ∼0.1, 100, 10, and 1,000, respectively, just before or at the initiation of the latest Permian extinction, but decreased to ∼0, 1, 1, and 10, respectively (Fig. 4d; Takahashi et al., 2014). These values implied an exhaustion of Mo, U, and V during this period. Mo and V are bioessential elements. For example, they are incorporated into metalloenzymes that control nitrogen fixation (Morel and Price, 2003). Takahashi et al. (2014) argued that high values of $Mo_{EF}$, $U_{EF}$, and $V_{EF}$ (reaching several thousand) in deep-sea sediments could have resulted in the drawdown of these trace elements from the global oceanic inventory. If this was indeed the case, the values of the authigenic redox-sensitive elements $Mo_{EF}$, $U_{EF}$, and $V_{EF}$ should have been limited by a contemporaneous decrease in their availability, even if oxygen-poor water conditions existed after the latest Permian extinction event. Xiang et al. (2016) reported low Mo and V contents in the sediments above the extinction horizon from Shangsi. In this section, peaks of high TOC (3%) and pyrite Fe per reactive Fe (80%) in the earliest Triassic horizon suggested reduced conditions, but the Mo concentration increased only to 1 ppm. These behaviors could have been due to the drawdown of these trace elements. The values of $Mo_{EF}$, $U_{EF}$, and $V_{EF}$ in Huangzhishan, Bianzhonglu, and Shangsi after the latest Permian extinction were
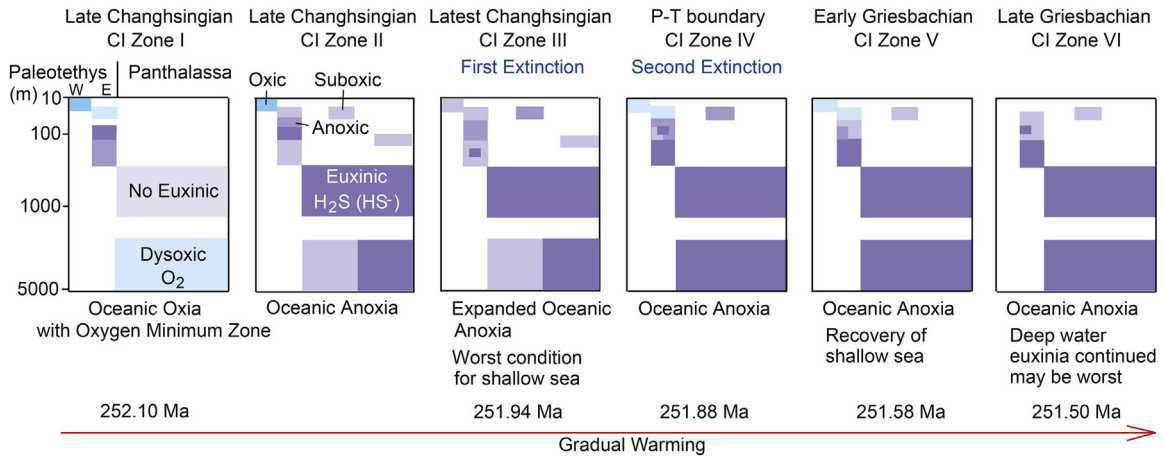
**Fig. 6.** Changes in redox conditions spanning the Permian-Triassic mass extinction in the Paleotethys and Panthalassa throughout the water column. Data sources are shown in Table 1. U/Pb dating of zircons after Burgess et al. (2014). Gradual warming after Sun et al. (2012). Anoxic and suboxic conditions shallower than 50 m could have occurred intermittently in the bottom water.

approximately 1/100, <1/1000, and 1/10 of the values before the extinction, although the occurrence of organic molecules and pyrite framboids indicated suboxic–anoxic conditions and related variation. These trends also suggested the exhaustion of Mo, U, and V in the surface water in Huangzhishan and Bianzhonglu during and after the latest Permian extinction. Source input of these trace elements to seawater would have increased, because the sedimentary accumulation rate around the continental margin increased 6- to 7-fold after the latest Permian extinction event (Algeo and Twitchett, 2010). Low $Mo_{EF}$ and $V_{EF}$ values despite a
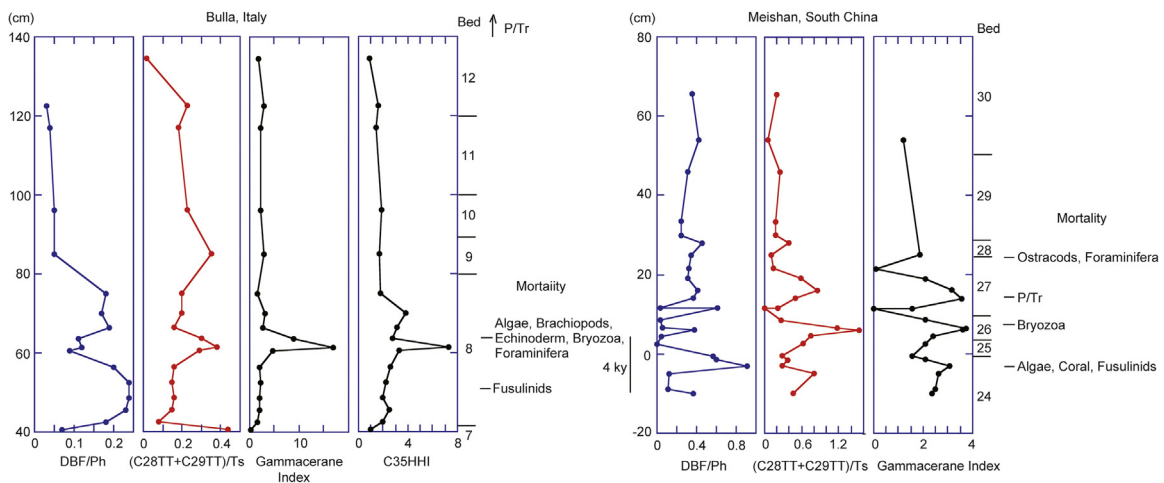


**Fig. 7.** Stratigraphic variation in dibenzofuran/phenanthrene, [C28TT + C29TT]/Ts, gammacerane index, and C35 homohopane index through the latest Permian extinction, accompanied by extinction horizons of some marine invertebrates at Bulla and Meishan. The marine mortality horizon at Bulla is after Gorjan et al. (2007) and that at Meishan is after Kaiho et al. (2006).

high source input demonstrated the significance of Mo and V deposition during anoxic ocean development at the latest Permian extinction.

Our new findings of significant decreases in $Mo_{EF}$ and $V_{EF}$ in shallower waters during and after the latest Permian extinction are consistent with limitations of bioessential elements not only in deep water but also in surface water.

## 4.12. Causes of extinctions

### 4.12.1. Soil/rock erosion and algal bloom

The extinction of land plants detected in terrestrial sections in South China occurred gradually, prior to (5–10 m below the negative shift of the $\delta^{13}C_{org}$) and coincidentally with it (Zhang et al., 2015). The negative shift in $\delta^{13}C_{org}$ in non-marine sediments corresponded to the negative shift of $\delta^{13}C_{carb}$. The first phase of marine extinction coincided with the negative shift of $\delta^{13}C_{carb}$. Vegetation loss could have occurred prior to the latest Permian extinction due to aerosol formation in the stratosphere (Kaiho et al., 2016) caused by Siberian volcanism, but associations between these events have yet to be confirmed. The loss of land vegetation could have induced massive soil and rock erosion, leading to the extinction of fusulinids, as the last occurrence and extinction of fusulinids occur in the maxima of DBF/Phe (Fig. 7). Muddy opaque seawater, which developed near the coast at this time, could have induced extinction of fusulinids and corals. After 4 kyr, transparent seawater dominated by nutrients appeared, resulting in high primary productivity, algal blooms, and oxygen-depleted water. The extinction horizons of algae, brachiopods, echinoderms, bryozoa, and foraminifera occurred at 21–24 cm of Bed 8 at Bulla during the maximum of the (C28TT + C29TT)/Ts ratio. The significant algal blooms could have induced a large number of harmful effects on organisms (the release of toxic components, asphyxiation through mechanical damage to tissues, etc.), $O_2$ deficiency at the sediment surface near the coast, and the extinctions.

The decrease in atmospheric oxygen concentration and $H_2S$ intrusion from intermediate water to surface water accompanied by an expansion of the OMZ may have also contributed to the $O_2$ deficiency. The high TOC during the latest Permian extinction in Bulla, Huangzhishan, and Meishan (Gorjan et al., 2007; Kaiho et al., 2006; Kaiho et al., 2012; Cao et al., 2009) can be attributed to algal blooms. The bloom event lasted for a few kyr and coincided with oceanic anoxia marked by the gammacerane and C35 homohopane indexes and the last occurrence of invertebrate fossils in the thin sections at Bulla and Meishan (Kaiho et al., 2006; Gorjan et al., 2007; Song et al., 2013; Fig. 7).

The massive soil intrusion into the ocean itself may have caused the extinction of marine sedentary organisms (Kaiho et al., 2013). The high flux of soil-derived
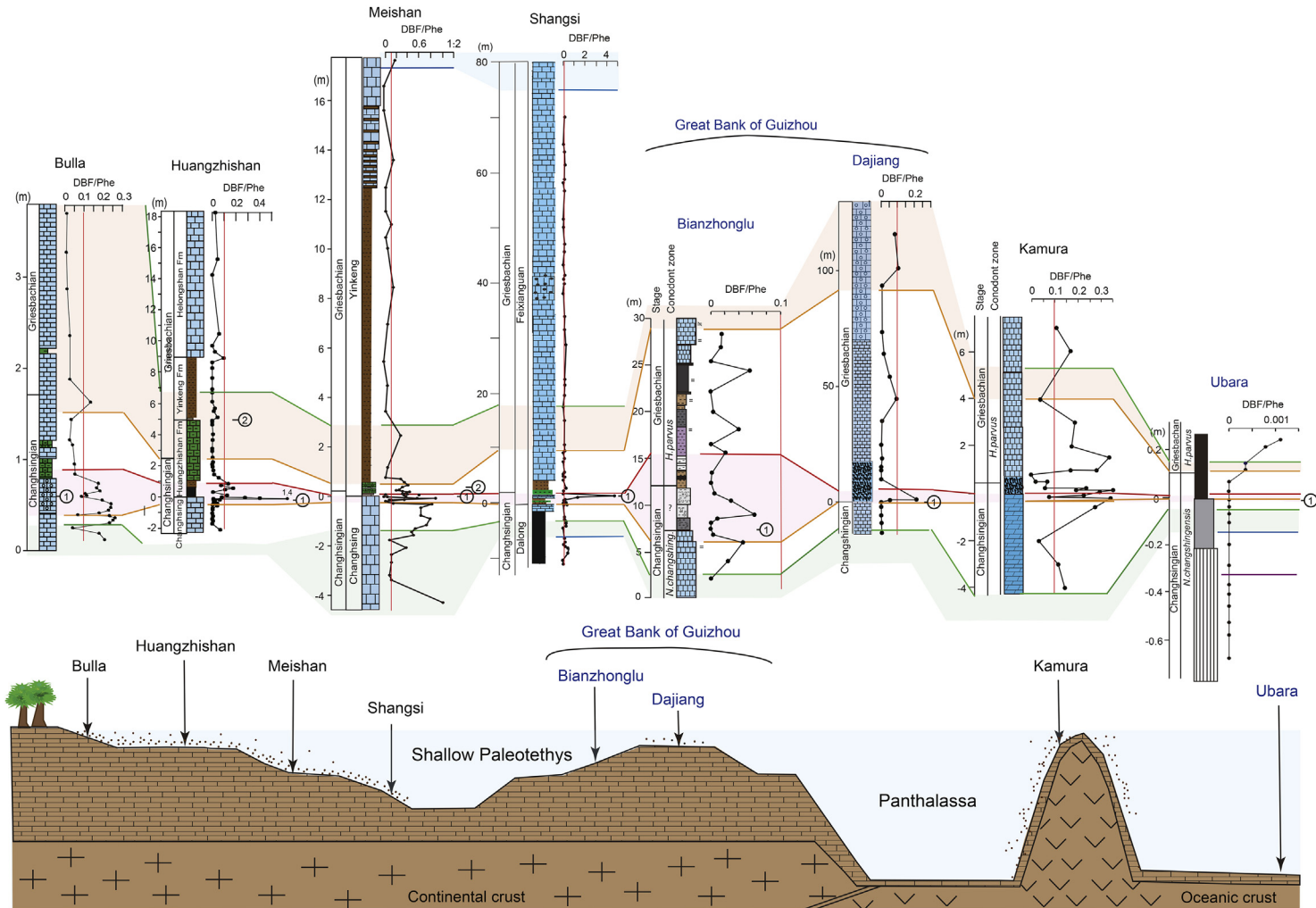
**Heliyon**

**Fig. 8.** Stratigraphic variation in hydrocarbon-derived geochemical parameters diagnostic for soil erosion (dibenzofurans) spanning the Permian-Triassic mass extinction in eight sections in Italy, South China, and Japan. A model cross-section in the Paleotethys and Panthalassa indicating distribution of soil intrusion into the sea during the latest Permian extinction is also shown corresponding to the stratigraphic distribution of the DBF/Phe values of the sections.

nutrients and the enormous mud supply from land to sea caused eutrophication (Murphy et al., 2000) and intermittent anoxia in nearshore waters. The high TOC values in CI Zone III in nearshore sections of Huangzhishan and Meishan (Kaiho et al., 2012) may have been due to algal blooms. Support for this scenario comes from the lack of a soil erosion event accompanied by an anoxic event in Bianzhonglu, the isolated platform, and its presence in nearshore sections. Furthermore, the net result of excessive fine sediment on reefs was a reduction in calcification, decreased recruitment, altered species composition, shallower depth distribution limits, and a loss of biodiversity (Fabricius, 2005). Corals are generally not found in areas where suspended sediment exceeds 10 mg/L, and high concentrations of sediment can injure corals (Ogston et al., 2004). Our hypothesis is consistent with the highly selective decimation of shallow-water sedentary organisms, such as reef-building corals and fusulinids (Chen and Benton, 2012). The extinction of benthic detritus feeders was more likely caused by intermittent algal blooms and oxygen deficiency accompanied by increasing seawater temperature.

### 4.12.2.  $O_2$ deficiency in shallow waters

An intrusion of euxinic water from the intermediate to the surface water (Gorjan et al., 2007; Kaiho et al., 2012) does not explain why the latest Permian (first-phase) extinction occurred in shallow surface waters because the wind mixed the surface layer, thus establishing it at the top 80–100 m, according to several models (Meyer et al., 2008; Ozaki et al., 2011; Monteiro et al., 2012). This also led to a shallower mixed layer depth, as shown in another model (French et al., 2015), such that the shallow surface waters should have remained oxygenated. $O_2$ deficiency in shallow waters should have been intermittent under the high partial pressure of $O_2$ in the Phanerozoic atmosphere. The latest Permian soil/rock erosion event accompanied by algal bloom inducing anoxia in surface sediments lasted for a short time, marked by a spike recorded in a 10-cm-thick sedimentary rock layer in each section.

The acidification of surface water in upwelling areas, estimated based on Ca isotope data (Payne et al., 2010; Clapham and Payne, 2011; Payne and Clapham, 2012), would have allowed $H_2S$ release into the atmosphere (a pH < 7 may have been possible in upwelling areas). $H_2S$ release from the intermediate waters and $CH_4$ release by the combustion of coal during the period of Siberian volcanism, which included an activity zone equivalent to half the area of Australia, caused a 10–14% decrease in the atmospheric oxygen concentration, resulting in a decrease from ~20% $O_2$ to ~18% $O_2$ in the air (Kaiho and Koga, 2013). The decrease in atmospheric oxygen is not sufficient to explain the latest Permian extinctions. Rather, other gases (e.g., $SO_2$; Svensen et al., 2009) may have also contributed to the decrease in oxygen. The decrease could have contributed to the rapid decrease

in oxygen levels in shallow surface waters. However, this would also have been insufficient to cause the latest Permian extinction.

### 4.12.3. Exhaustion of bioessential elements

Mo and V were exhausted in the surface waters during and just after the latest Permian extinction, as evidenced in Huangzhishan and reported here (Fig. 4d). The exhaustion may have contributed the latest Permian (first-phase) marine extinction in the surface waters because Mo and V are essential elements for primary producers and animals (Takahashi et al., 2014).

### 4.12.4. Earliest Triassic (second-phase) extinction

The oxic conditions in shallow surface waters in the Paleotethys in CI Zone IV cannot explain the second phase of the marine extinction. The second-phase extinction had no soil/rock erosion and algal bloom event. The culmination of intermediate water anoxia occurred during the span of the second-phase extinction. According to the $\delta^{18}O_{\text{apatite or brachiopod carbonate}}$ data of Sun et al. (2012), Joachimski et al. (2012), Brand et al. (2012), Schobben et al. (2014), and Chen et al. (2016), surface seawater temperature increases occurred spanning the first- and second-phase extinctions. $P_{CO2}$ would be expected to increase gradually in parallel with the temperature increases, leading to a decrease in the pH of seawater. Excessive acid rainfall associated with emplacement of the Siberian Traps magmatic province occurred spanning the first- and second-phase extinctions (Sephton et al., 2015). Rapid and large injections of carbon and sulfur caused an abrupt acidification event (pH 7.4–7.6) that drove the preferential loss of heavily calcified marine biota. The high $P_{CO2}$, high surface-water temperature (ca. 35 °C), acidification of seawater (pH 7.4–7.6), and culmination of intermediate water anoxia (this study) could have been the main causes of the second-phase extinction.

## 5. Conclusions

Three important findings resulted from this study. One is a soil and rock erosion event causing significant algal blooms and a significant intermittent decrease in free oxygen in shallow nearshore bottom water in the low-latitude sea at the latest Permian extinction horizon. The second is that the vertical ocean redox structure at low latitudes changed from a well-mixed oxic to a stratified euxinic–anoxic ocean beginning immediately prior to the first-phase extinction and continuing over a period of approximately one million years after the latest Permian extinction. The third finding is a loss of bioessential elements in the surface water at the latest Permian extinction. Siberian volcanism may have induced the loss of land vegetation by producing aerosols that accumulated in the stratosphere. This was followed by an increase in greenhouse gases, warming, the latest Permian

extinction, and thus the second-phase extinction. The excess supply of nutrients leading to algal blooms in the warm climate could have caused environmental stress to shallow water animals, which could have contributed to the first-phase extinction, along with the high temperature and low pH of the surface waters. However, the cause of the second-phase extinction was not excess supply of sediments and nutrients but rather enhanced global warming, ocean acidification, hypercapnia, and oceanic euxinia–anoxia.

## Declarations

### Author contribution statement

Kunio Kaiho: Conceived and designed the experiments; Performed the experiments; Analyzed and interpreted the data; Contributed reagents, materials, analysis tools or data; Wrote the paper.

Ryosuke Saito, Kosuke Ito, Takashi Miyaji, Raman Biswas, Lei Liang, Fumiko W. Nara: Performed the experiments.

Li Tian, Hiroyoshi Sano, Zhiqiang Shi, Satoshi Takahashi, Jinnan Tong, Masahiro Oba, Noriyoshi Tsuchiya, Zhong-Qiang Chen: Contributed reagents, materials, analysis tools or data.

### Funding statement

### Competing interest statement

The authors declare no conflict of interest.

### Additional information

Supplementary content related to this article has been published online at
http://dx.doi.org/10.1016/j.heliyon.2016.e00137

### Acknowledgments

# References

Ahmed, M., George, S.C., 2004. Changes in the molecular composition of crude oils during their preparation for GC and GC–MS analyses. Org. Geochem. 35, 137–155.

Algeo, T.J., Hinnov, L., Moser, J., Barry Maynard, J., Elswick, E., Kuwahara, K., Sano, H., 2010. Changes in productivity and redox conditions in the Panthalassic Ocean during the latest Permian. Geology 38, 187–190.

Algeo, T.J., Kuwahara, K., Sano, H., Bates, S., Lyons, T., Elswick, E., Hinnov, L., Ellwood, B., Moser, J., Maynard, J.B., 2011. Spatial variation in sediment fluxes, redox conditions, and productivity in the Permian– Triassic Panthalassic Ocean. Palaeogeogr. Palaeoclimatol. Palaeoecol. 308, 65–83.

Algeo, T.J., Maynard, J.B., 2004. Trace-element behavior and redox facies in core shales of Upper Pennsylvanian Kansas-type cyclothems. Chem. Geol. 206, 289–318.

Algeo, T.J., Twitchett, R.J., 2010. Anomalous Early Triassic sediment fl uxes due to elevated weathering rates and their biological consequences. Geology 38, 1023–1026.

Asif, M., Alexander, R., Fazeelat, T., Pierce, K., 2009. Geosynthesis of dibenzothiophene and alkyl dibenzothiophenes in crude oils and sediments by carbon catalysis. Org. Geochem. 40, 895–901.

Brumsack, H.-J., 2006. The trace metal content of recent organic carbon-rich sediments: Implications for Cretaceous black shale formation. Palaeogeogr. Palaeoclimatol. Palaeoecol. 232, 344–361.

Burgess, S.D., Bowring, S., Shen, S.-Z., 2014. High-precision timeline for Earth's most severe extinction. Proc. Natl. Acad. Sci. USA 111, 3316–3321.

Brand, U., Posenato, R., Came, R., Affek, H., Angiolini, L., Azmy, K., Farabegoli, E., 2012. The end-Permian mass extinction: A rapid volcanic $CO_2$ and $CH_4$-climatic catastrophe. Chem. Geol. 322-323, 121–144.

Brosse, M., Bucher, H., Goudemand, N., 2016. Quantitative biochronology of the Permian–Triassic boundary in South China based on conodont unitary associations. Earth-Sci. Rev. 155, 153–171.

Cao, C., Love, G.D., Hays, L.E., Wang, W., Shen, S., Summons, R.E., 2009. Biogeochemical evidence for euxinic oceans and ecological disturbance presaging the end-Permian mass extinction event. Earth Planet Sci. Lett. 281, 188–201.

Chen, J., Shen, S.Z., Li, X.H., Xu, Y.G., Joachimski, M.M., Bowring, S.A., Erwin, D.H., Yuan, D., Chen, B., Zhang, H., Wang, Y., Cao, C., Zheng, Q., Mu, L., 2016.

High-resolution SIMS oxygen isotope analysis on conodont apatite from South China and implications for the end-Permian mass extinction. Palaeogeogr. Palaeoclimatol. Palaeoecol. 448, 26–38.

Chen, Z.Q., Benton, M.J., 2012. The timing and pattern of biotic recovery following the end-Permian mass extinction. Nat. Geosci. 5, 375–383.

Chen, Z.Q., Tong, J.N., Zhang, K., Yang, H., Liao, Z., Song, H., Chen, J., 2009. Environmental and biotic turnover across the Permian–Triassic boundary on a shallow carbonate platform in western Zhejiang, South China. Aust. J. Earth Sci. 56, 775–797.

Chen, Z.Q., Tong, J.N., Liao, Z.T., Chen, J., 2010. Structural changes of marine communities over the Permian–Triassic transition: ecologically assessing the end-Permian mass extinction and its aftermath. Global Planet. Change 73, 123–140.

Chen, Z.Q., Tong, J., Fraiser, M.L., 2011. Trace fossil evidence for restoration ofmarine ecosystems following the end-Permian mass extinction in the Lower Yangtze region South China. Palaeogeogr. Palaeoclimatol. Palaeoecol. 299, 449–474.

Clarkson, M.O., Kasemann, S.A., Wood, R.A., Lenton, T.M., Daines, S.J., Richoz, S., Ohnemueller, F., Meixner, A., Poulton, S.W., Tipper, E.T., 2015. Ocean acidification and the Permo-Triassic mass extinction. Science 2015 (348), 229–232.

Clapham, M.E., Payne, J.L., 2011. Acidification, anoxia, and extinction: a multiple logistic regression analysis of extinction selectivity during the Middle and Late Permian. Geology 39, 1059–1062.

Didyk, B.M., Simoneit, B.R.T., Brassell, S.C., Eglinton, G., 1978. Organic geochemical indicators of palaeoenvironmental conditions of sedimentation. Nature 272, 216–222.

Ehrenberg, S.N., Svana, T.A., Swart, P.K., 2008. Uranium depletion across the Permian-Triassic boundary in Middle East carbonates: Signature of oceanic anoxia. AAPG Bulletin 92, 691–707.

Fabricius, K.E., 2005. Effects of terrestrial runoff on the ecology of corals and coral reefs; review and synthesis. Mar. Pollut. Bull 50, 125–146.

Farabegoli, E., Perri, M.C., Posenato, R., 2007. Environmental and biotic changes across the Permian-Triassic boundary in western Tethys: The Bulla parastratotype, Italy. Global Planet. Change 55, 109–135.

Feng, Q., Algeo, T.J., 2014. Evolution of oceanic redox conditions during the Permo-Triassic transition: Evidence from deepwater radiolarian facies. Earth Sci. Rev. 137, 34–51.

French, K.L., Rocher, D., Zumberge, J.E., Summons, R.E., 2015. Assessing the distribution of sedimentary C40 carotenoids through time. Geobiology 13, 139–151.

Gorjan, P., Kaiho, K., Kakegawa, T., Niitsuma, S., Chen, Z.Q., Kajiwara, Y., Nicora, A., 2007. Paleoredox, biotic and sulfur-isotopic changes associated with the end-Permian mass extinction in the western Tethys. Chem. Geol. 244, 483–492.

Goossens, H., de Leeuw, J.W., Schenck, P.A., Brassell, S.C., 1984. Tocopherols as likely precursors of pristane in ancient sediments and crude oils. Nature 312, 440–442.

Grice, K., Cao, C., Love, G.D., Bottcher, M.E., Twitchett, R.J., Grosjean, E., Summons, R.E., Turgeon, S.C., Dunning, W., Jin, Y., 2005. Photic zone euxinia during the Permian–Triassic superanoxic event. Science 307, 706–709.

Holba, A.G., Dzou, L.I., Hallam, A., Masterson, W.D., Francu, J., Fincannon, A.L., 2001. Extended tricyclic terpanes as age discriminators between Triassic, Early Jurassic, and Middle-Late Jurassic oils. 20th International Meeting on Organic Geochemistry: EAOG 1, Nancy, France., 464.

Horacek, M., Koike, T., Richoz, S., 2009. Lower Triassic $\delta^{13}C$ isotope curve from shallow-marine carbonates in Japan, Panthalassa realm: Confirmation of the Tethys $\delta^{13}C$ curve. J. Asian Earth Sci. 36, 481–490.

Hughes, W.B., Holba, A.G., Dzou, L.I.P., 1995. The ratios of dibenzothiophene to phenanthrene and pristine to phytane as indicators of depositional environment and lithology of petroleum source rocks. Geochim. Cosmochim. Acta 59, 3581–3598.

Jin, Y.G., Wang, Y., Wang, W., Shang, Q.H., Cao, C.Q., Erwin, D.H., 2000. Pattern of marine mass extinction near the Permian-Triassic boundary in south China. Science 289, 432–436.

Joachimski, M.M., Lai, X., Shen, S., Jiang, H., Luo, G., Chen, B., Chen, J., Sun, Y., 2012. Climate warming in the latest Permian and the Permian–Triassic mass extinction. Geology 40, 195–198.

Kaiho, K., Kajiwara, Y., Chen, Z.Q., Gorjan, P., 2006. A sulfur isotope event at the end of the Permian. Chem. Geol. 235, 33–47.

Kaiho, K., Koga, S., 2013. Impacts of a massive release of methane and hydrogen sulfide on oxygen and ozone during the late Permian mass extinction. Global Planet. Change 107, 91–101.

Kaiho, K., Oba, M., Fukuda, Y., Ito, K., Ariyoshi, S., Gorjan, P., Riu, Y., Takahashi, S., Chen, Z.Q., Tong, J., Yamakita, S., 2012. Changes in depth-transect redox conditions spanning the end-Permian mass extinction and their impact on the

marine extinction: Evidence from biomarkers and sulfur isotopes. Global Planet. Change 94-95, 20–32.

Kaiho, K., Oshima, N., Adachi, K., Adachi, Y., Mizukami, T., Fujibayashi, M., Saito, R., 2016. Global climate change driven by soot at the K-Pg boundary as the cause of the mass extinction. Sci. Rep. 6, 28427. www.nature.com/articles/srep28427.

Kaiho, K., Yatsu, S., Oba, M., Gorjan, P., Casier, J.-G., Ikeda, M., 2013. A forest fire and soil erosion event during the Late Devonianmass extinction. Palaeogeogr. Palaeoclimatol. Palaeoecol. 392, 272–280.

Kasprak, A.H., Sepúlveda, J., Price-Waldman, R., Williford, K.H., Schoepfer, S.D., Haggart, J.W., Ward, P.D., Summons, R.E., Whiteside, J.H., 2015. Episodic photic zone euxinia in the northeastern Panthalassic Ocean during the end-Triassic extinction. Geology 43, 307–310.

Kasuya, A., Isozaki, Y., Igo, H., 2012. Constraining paleo-latitude of a biogeographic boundary in mid-Panthalassa: Fusuline province shift on the Late Guadalupian (Permian) migrating seamount. Gondwana Res. 21, 611–623.

Killops, S., Killops, V., 2005. Introduction to Organic Geochemistry, Second Edition Blackwell Publishing, Malden, MA.

Knoll, A.H., Bambach, R.K., Payne, J.L., Pruss, S., Fischer, W.W., 2007. Paleophysiology and end-Permian mass extinction. Earth Planet. Sci. Lett. 256, 295–313.

Koike, T., 1996. The first occurrence of Griesbachian conodonts in Japan. Trans. Paleont. Soc. Japan (New Series) 181, 337–346.

Koopmans, M.P., Rijpstraa, W.I.C., Klapwijka, M.M., de Leeuwa, J.W., Lewanb, M.D., Sinninghe Damste, J.S., 1999. A thermal and chemical degradation approach to decipher pristane and phytane precursors in sedimentary organic matter. Org. Geochem. 30, 1089–1104.

Kump, L.R., Pavlov, A., Arthur, M.A., 2005. Massive release of hydrogen sulfide to the surface ocean and atmosphere during intervals of oceanic anoxia. Geology 33, 397–400.

Laflamme, R.E., Hites, R.A., 1978. The global distribution of polycyclic aromatic hydrocarbons in recent sediments. Geochim. Cosmochim. Acta 42, 289–303.

McLennan, S., 2001. Relationships between the trace element composition of sedimentary rocks and upper continental crust. Geochem. Geophys. Geosyst. 2 (4).

Meyer, K., Kump, L., Ridgwell, A., 2008. Biogeochemical controls on photic-zone euxinia during the end-Permian mass extinction. Geology 36, 747–750.

Monteiro, F.M., Pancost, R.D., Ridgewell, A., Donnadieu, Y., 2012. Nutrients as the dominant control on the spread of anoxia and euxinia across the Cenomanian-Turonian oceanic anoxic event (OAE2): model-data comparison. Paleoceanography 27, PA002351.

Morel, F.M.M., Price, N.M., 2003. The Biogeochemical Cycles of Trace Metals in the Oceans. Science 300, 944–947.

Murphy, A.E., Sageman, B.B., Hollander, D.J., 2000. Eutrophication by decoupling of the marine biogeochemical cycles of C, N, and P: A mechanism for the Late Devonian mass extinction. Geology 28, 427–430.

Musashi, M., Isozaki, Y., Koike, T., Kreulen, R., 2001. Stable carbon isotope signature in mid-Panthalassa shallow-water carbonates across the Permo-Triassic boundary: evidence for $^{13}$C-depleted superocean. Earth Planet. Sci. Lett. 191, 9–20.

Nabbefeld, B., Grice, K., Summons, R.E., Hays, L.E., Cao, C., 2010. Significance of polycyclic aromatic hydrocarbons (PAHs) in Permian/Triassic boundary sections. Appl. Geochem. 25, 1374–1382.

Ogston, A.S., Storlazzi, C.D., Field, M.E., Presto, M.K., 2004. Sediment resuspension and transport patterns on a fringing reef fla. Molokai, Hawaii. Coral Reefs 23, 559–569.

Okai, T., Suzuki, A., Terashima, S., Inoue, M., Nohara, M., Kawahata, H., Imai, N., 2004. Collaborative analysis of GSJ/AIST geochemical reference materials JCp-1 (Coral) and JCt-1(Giant Clam). Chikyu Kagaku 38, 281–286.

Ozaki, K., Tajima, S., Tajika, E., 2011. Conditions required for oceanic anoxia/euxinia: constraints from a one-dimensional ocean biogeochemical cycle model. Earth Planet. Sci. Lett. 304, 270–279.

Payne, J.L., Clapham, M.E., 2012. End-Permian Mass extinction in the Oceans: an Ancient Analog for the Twenty-First Century? Annu. Rev. Earth Planet. Sci. 40, 89–111.

Payne, J.L., Lehrmann, D.J., Wei, J., Orchard, M.J., Schrag, D.P., Knoll, A.H., 2004. Large perturbations of the Carbon cycle Dduring recovery from the end-Permian extinction. Science 305, 506–509.

Payne, J.L., Turchyn, A.V., Paytan, A., DePaolo, D.J., Lehrmann, D.J., Yu, M., Wei, J., 2010. Calcium isotope constraints on the end-Permian mass extinction. Proc. Natl. Acad. Sci. USA 107, 8543–8548.

Peters, K.E., Moldowan, J.M., 1991. Effects of source, thermal maturity, and biodegradation on the distribution and isomerization of homohopanes in petroleum. Org. Geochem. 17, 47–61.

Peters, K.E., Walters, C.C., Moldowan, J.M., 2005. The Biomarker Guide. Cambridge University Press, Cambridge, pp. 1155.

Raiswell, R., Buckley, F., Berner, R.A., Anderson, T.F., 1988. Degree of pyritization of iron as a paleoenvironmental indicator of bottom-water oxygenation. J. Sediment. Petrol. 58, 812–819.

Rampino, M.R., Prokoph, A., Adler, A.C., Schwindt, D.M., 2002. Abruptness of the end-Permian mass extinction as determined from biostratigraphic and cyclostratigraphic analyses of European western Tethyan sections. In: Koeberl, C., MacLeod, K.G. (Eds.), Catastrophic Events and Mass Extinctions: Impacts and Beyond. Geological Society of America, Boulder, pp. 415–427.

Rashid, M.A., 1979. Pristane-phytane ratios in relation to source and diagenesis of ancient sediments from the Labrador shelf. Chem. Geol. 25, 109–122.

Riccardi, A.L., Kump, L.R., Arthur, M.A., D'Hondt, S., 2007. Carbon isotopic evidence for chemocline upward excursions during the end-Permian event. Palaeogeogr. Palaeoclimatol. Palaeoecol. 248, 73–81.

Rontani, J.-F., Bonin, P., Vaultier, F., Guasco, S., Volkman, J.K., 2013. Anaerobic bacterial degradation of pristenes and phytenes in marine sediments does not lead to pristane and phytane during early diagenesis. Org. Geochem. 58, 43–55.

De Rosa, M., Gambacorta, A., 1988. The lipids of archaebacteria. Prog. Lipid Res. 27, 153–175.

Schobben, M., Joachimski, M.M., Korn, D., Leda, L., Korte, C., 2014. Palaeotethys seawater temperature rise and an intensified hydrological cycle following the end-Permian mass extinction. Gondwana Res. 26, 675–683.

Schobben, M., Stebbins, A., Ghaderic, A., Straussd, H., Korna, D., Korte, C., 2015. Flourishing ocean drives the end-Permian marine mass extinction. Proc. Natl. Acad. Sci. USA 112, 10298–10303.

Schoepfer, S.D., Henderson, C.M., Garrison, G.H., Foriel, J., Ward, P.D., Selby, D., Hower, J.C., Algeo, T.J., Shen, Y., 2013. Termination of a continent-margin upwelling system at the Permian–Triassic boundary (Opal Creek, Alberta, Canada). Global Planet. Change 105, 21–35.

Sephton, M.A., Jiao, D., Engel, M.H., Looy, C.V., Visscher, H., 2015. Terrestrial acidification during the end-Permian biosphere crisis? Geology 43, 159–162.

Sephton, M.A., Looy, C.V., Brinkhuis, H., Wignall, P.B., de Leeuw, J.W., Visscher, H., 2005. Catastrophic soil erosion during the end-Permian biotic crisis. Geology 33, 941–944.

Shen, S.Z., Cao, C.Q., Zhang, H., Bowring, S.A., Henderson, C.M., Payne, J.L., Davydov, V.I., Chen, B., Yuan, D., Zhang, Y., Wang, W., Zheng, Q., 2013. High-resolution $\delta^{13}C_{carb}$ chemostratigraphy from latest Guadalupian through earliest Triassic in South China and Iran. Earth Planet. Sci. Lett. 375, 156–165.

Sinninghe Damsté, J.S., Kenig, F., Koopmans, M.P., Köster, J., Schouten, S., Hayes, J.M., de Leeuw, J.W., 1995. Evidence for gammacerane as an indicator of water column stratification. Geochim. Cosmochim. Acta 59, 1895–1900.

Sivan, P., Datta, G.C., Singh, R.R., 2008. Aromatic biomarkers as indicators of source, depositional environment, maturity and secondary migration in the oils of Cambay Basin, India. Org. Geochem. 39, 1620–1630.

Soldan, A.L., Cerqueira, J.R., 1986. Effects of thermal maturation on geochemical parameters obtained by simulated generation of hydrocarbons. Org. Geochem. 10, 339–345.

Song, H., Wignall, P.B., Chu, D., Tong, J., Sun, Y., Song, H., He, W., Tian, L., 2014. Anoxia/high temperature double whammy during the Permian-Triassic marine crisis and its aftermath. Sci. Rep. 4, 4132.

Song, H., Wignal, P.B., Tong, J., Yin, H., 2013. Two pulses of extinction during the Permian–Triassic crisis. Nat. Geosci. 6, 52–56.

Sun, Y., Joachimski, M.M., Wignall, P.B., Yan, C., Chen, Y., Jiang, H., Lina Wang, L., Lai, X., 2012. Lethally hot temperatures during the Early Triassic greenhouse. Science 338, 366–370.

Summons, R.E., 1993. Biogeochemical cycles: a review of fundamental aspects of organic matter formation, preservation, and composition. In: Engel, M.H., Macko, S.A. (Eds.), Organic Geochemistry—Principles and Applications. Plenum Press, New York, pp. 3–21.

Summons, R.E., Powell, T.G., 1987. Identification of aryl isoprenoids in source rocks and crude oils: Biological markers for the green sulphur bacteria. Geochim. Cosmochim. Acta 51, 557–566.

Summons, R.E., Jahnke, L.L., 1990. Identification of the methylhopanes in sediments and petroleum. Geochim. Cosmochim. Acta 54, 247–251.

Svensen, H., Planke, S., Polozov, A.G., Schmidbauer, N., Corfu, F., Yuri, Y., Podladchikov, Y.Y., Jamtveit, B., 2009. Siberian gas venting and the end-Permian environmental crisis. Earth Planet. Sci. Lett. 277, 490–500.

Tada, R., Watanabe, S., Kashiyama, Y., Tajika, E., Kato, T., Yamamoto, S., Isozaki, Y., Sakuma, H., 2005. High-resolution analysis of Late Paleozoic–Early Mesozoic variability of paleoceanographic system recorded inbedded chert sequence in the inner zone of Southwest Japan. J. Geogr. 114, 638–642 (in Japanese).

Takahashi, S., Kaiho, K., Oba, M., Kakegawa, T., 2010. A smooth negative shift of organic-carbon isotope ratios at an end-Permian mass extinction horizon in central pelagic Panthalassa. Palaeogeogr. Palaeoclimatol. Palaeoecol. 292, 532–539.

Takahashi, S., Yamakita, S., Suzuki, N., Kaiho, K., Ehiro, M., 2009. High organic carbon content and a decrease in radiolarians at the end of the Permian in a newly discovered continuous pelagic section: a coincidence? Palaeogeogr. Palaeoclimatol. Palaeoecol. 271, 1–12.

Takahashi, S., Yamasaki, S., Ogawa, Y., Kimura, K., Kaiho, K., Yoshida, T., Tsuchiya, N., 2014. Bioessential element-depleted ocean following the euxinic maximum of the end-Permian mass extinction. Earth Planet. Sci. Lett. 393, 94–104.

Takishita, K., Chikaraishi, Y., Leger, M.M., Kim, E., Yabuki, A., Ohkouchi, N., Roger, A.J., 2012. Lateral transfer of tetrahymanol-synthesizing genes has allowed multiple diverse eukaryote lineages to independently adapt to environments without oxygen. Biol. Direct, 7.

Tang, Y.C., Staauffer, M., 1995. Formation of pristene, pristane and phytane: kinetic study by laboratory pyrolysis of Monterey source rock. Org. Geochem. 23, 451–460.

Tian, L., Tong, J.N., Algeo, T.J., et al., 2014. Reconstruction of Early Triassic Ocean Redox Conditions Based on Framboidal Pyrite from the Nanpanjiang Basin, South China. Palaeogeogr. Palaeoclimatol. Palaeoecol. 412, 68–79.

Tribovillard, N., Algeo, T.J., Lyons, T., Riboulleau, A., 2006. Trace metals as paleoredox and paleoproductivity proxies: An update. Chem. Geol. 232, 12–32.

Van Gemerden, H., Mas, J., et al., 1995. Ecology of phototrophic sulfur bacteria. In: Blankenship, R.E. (Ed.), Anoxygenic Photosynthetic Bacteria. Kluwer Academic Publishers, Dordrecht, pp. 49–85.

Wakeham, S.G., Schaffner, C., Giger, W., 1980. Polycyclic aromatic hydrocarbons in Recent lake sediments I. Compounds having anthropogenic origarns. Geochim. Cosmochim. Acta 44, 403–413.

Wang, L., Wignall, P.B., Wang, Y., Jiang, H., Sun, Y., Guoshan Li, G., Yuan, J., Lai, X., 2016. Depositional conditions and revised age of the Permo-Triassic microbialites at Gaohua section Cili County (Hunan Province. South China). Palaeogeogr. Palaeoclimatol. Palaeoecol. 443, 156–166.

Wignall, P.B., Bond, D.P.G., Kuwahara, K., Kakuwa, Y., Newton, R.J., Poulton, S. W., 2010. An 80 million year oceanic redox history from Permian to Jurassic pelagic sediments of the Mino-Tamba terrane, SW Japan, and the origin of four mass extinctions. Global Planet. Change 71, 109–123.

Wignall, P.B., Hallam, A., Xulong, L., Fengqing, Y., 1995. Palaeoenvironmental changes across the Permian/Triassic boundary at Shangsi (N. Sichuan China). Hist. Biol. 10, 175–189.

Wignall, P.B., Newton, R., 1998. Pyrite framboid diameter as a measure of oxygen deficiency in ancient mudrocks. Am. J. Sci. 298, 537–552.

Wilkin, R.T., Barnes, H.L., 1997. Formation processes of framboidal pyrite. Geochim. Cosmochim. Acta 61, 323–339.

Wilkin, R.T., Barnes, H.L., Brantley, S.L., 1996. The size distribution of framboidal pyrite in modern sediments: an indicator of redox conditions. Geochim. Cosmochim. Acta 60, 3897–3912.

Xiang, L., Schoepfer, S.D., Zhang, H., Yuan, D.X., Cao, C.Q., Zheng, Q.F., Henderson, C.M., Shen, S.Z., 2016. Oceanic redox evolution across the end-Permian mass extinction at Shangsi South China. Palaeogeogr. Palaeoclimatol. Palaeoecol. 448, 59–71.

Xie, S., Pancost, R.D., Huang, J., Wignall, P.B., Yu, J., Tang, X., Chen, L., Huang, X., Lai, X., 2007b. Changes in the global carbon cycle occurred as two episodes during the Permian–Triassic crisis. Geology 35, 1083–1086.

Yamakita, S., Kakuwa, N., Kato, T., Tada, R., Ogihara, S., Tajika, E., Hamada, Y., 1999. Confirmation of the Permian/Triassic boundary in deep-sea sedimentary rocks; earliest Triassic conodonts from black carbonaceous claystone of the Ubara section in the Tamba Belt, Southwest Japan. J. Geol. Soc. Japan 105, 895–898.

Yin, H., Jiang, H., Xia, W., Feng, Q., Zhang, N., Shen, J., 2014. The end-Permian regression in South China and its implication on mass extinction. Earth-Sci. Rev. 137, 19–33.

Zhang, H., Cao, C., Liu, X., Mu, L., Zheng, Q., Liu, F., Xiang, L., Liu, L., Shen, S., 2015. The terrestrial end-Permian mass extinction in South China. Palaeogeogr. Palaeoclimatol. Palaeoecol. 448, 108–124.

Ziegler, A.M., Gibbs, M.T., Hulver, M.L., 1998. A mini-atlas of oceanic water masses in the Permian Period. Proc. R. Soc. Victoria 110, 323–344.